The Astrophysical Journal, 768:55 (20pp), 2013 May 1 doi:10.1088/0004-637X/768/1/55

HERSCHEL/SPIRE SUBMILLIMETER SPECTRA OF LOCAL ACTIVE GALAXIES*,†

Miguel Pereira-Santaella[1], Luigi Spinoglio[1], Gemma Busquet[1], Christine D. Wilson[2], Jason Glenn[3], Kate G. Isaak[4], Julia Kamenetzky[3], Naseem Rangwala[3], Maximilien R. P. Schirm[2], Maarten Baes[5], Michael J. Barlow[6], Alessandro Boselli[7], Asantha Cooray[8], and Diane Cormier[9]

[1] Istituto di Astrofisica e Planetologia Spaziali, INAF, Via Fosso del Cavaliere 100, I-00133 Roma, Italy; miguel.pereira@ifsi-roma.inaf.it
[2] Department of Physics and Astronomy, McMaster University, Hamilton, Ontario, L8S 4M1, Canada
[3] Center for Astrophysics and Space Astronomy, 389-UCB, University of Colorado, Boulder, CO 80303, USA
[4] ESA Astrophysics Missions Division, ESTEC, P.O. Box 299, 2200 AG Noordwijk, The Netherlands
[5] Sterrenkundig Observatorium, Universiteit Gent, Krijgslaan 281 S9, B-9000 Gent, Belgium
[6] Department of Physics and Astronomy, University College London, Gower Street, London WC1E 6BT, UK
[7] Laboratoire d'Astrophysique de Marseille (LAM), Universitè d'Aix-Marseille and CNRS, UMR7326, 38 rue F. Joliot-Curie, F-13388 Marseille Cedex 13, France
[8] Center for Cosmology, Department of Physics and Astronomy, University of California, Irvine, CA 92697, USA
[9] Laboratoire AIM, CEA/DSM-CNRS-Universitè Paris Diderot, Irfu/Service d'Astrophysique, CEA Saclay, F-91191 Gif-sur-Yvette, France

Received 2013 January 11; accepted 2013 March 13; published 2013 April 15

ABSTRACT

We present the submillimeter spectra from 450 to 1550 GHz of 11 nearby active galaxies observed with the SPIRE Fourier Transform Spectrometer (SPIRE/FTS) on board *Herschel*. We detect CO transitions from $J_{up} = 4$ to 12, as well as the two [C I] fine structure lines at 492 and 809 GHz and the [N II]1461 GHz line. We used radiative transfer models to analyze the observed CO spectral line energy distributions. The FTS CO data were complemented with ground-based observations of the low-J CO lines. We found that the warm molecular gas traced by the mid-J CO transitions has similar physical conditions ($n_{H_2} \sim 10^{3.2}$–$10^{3.9}$ cm^{-3} and $T_{kin} \sim 300$–800 K) in most of our galaxies. Furthermore, we found that this warm gas is likely producing the mid-IR rotational H_2 emission. We could not determine the specific heating mechanism of the warm gas, however, it is possibly related to the star formation activity in these galaxies. Our modeling of the [C I] emission suggests that it is produced in cold ($T_{kin} < 30$ K) and dense ($n_{H_2} > 10^3$ cm^{-3}) molecular gas. Transitions of other molecules are often detected in our SPIRE/FTS spectra. The HF $J = 1$–0 transition at 1232 GHz is detected in absorption in UGC 05101 and in emission in NGC 7130. In the latter, near-infrared pumping, chemical pumping, or collisional excitation with electrons are plausible excitation mechanisms likely related to the active galactic nucleus of this galaxy. In some galaxies, few H_2O emission lines are present. Additionally, three OH^+ lines at 909, 971, and 1033 GHz are identified in NGC 7130.

Key words: galaxies: active – galaxies: ISM – galaxies: nuclei – galaxies: Seyfert

Online-only material: color figures

1. INTRODUCTION

The submillimeter (sub-mm) is one of the few astronomical spectral regions that has not been fully explored so far. In part, this is because ground-based sub-mm observations are difficult due to the low transparency of the atmosphere. Consequently, only a small number of bright sources have been observed in a few atmospheric windows (350, 450, and 850 μm). The SPIRE Fourier Transform Spectrometer (SPIRE/FTS; Griffin et al. 2010; Naylor et al. 2010; Swinyard et al. 2010) on board the *Herschel Space Observatory* (Pilbratt et al. 2010) fills most of this gap, covering the spectral range between 450 and 1440 GHz (210 and 670 μm), and provides an important benchmark for high-redshift studies with the Atacama Large Millimeter/submillimeter Array.

Besides the continuum arising from cold dust, in the sub-mm range there are several molecular and atomic spectral lines that probe the different phases of the interstellar medium (ISM) in galaxies (e.g., van der Werf et al. 2010; Panuzzo et al. 2010; Rangwala et al. 2011). In the SPIRE/FTS spectral range, the most prominent spectral feature is the CO ladder from $J_{up} = 4$ to 13. CO is a good tracer of the molecular gas since it is one of the most abundant molecules in the ISM. In particular, these mid-J CO lines originate in warm molecular gas (their upper-level energies range from 55 to 500 K above the ground state) that can be excited by ultraviolet (UV) photons in photon-dominated regions (PDRs; e.g., Wolfire et al. 2010), X-rays in X-ray dominated regions (XDRs; e.g., Meijerink et al. 2006), or by shocks (e.g., Flower & Pineau Des Forêts 2010). The analysis of the CO spectral line energy distribution (SLED), including low- and mid-J CO transitions, is crucial for understanding the conditions in the cold and warm molecular gas, and the dominant heating mechanism in galaxies (Rangwala et al. 2011; Kamenetzky et al. 2012; Spinoglio et al. 2012).

In addition to the CO ladder, two [C I] fine structure lines are present in the sub-mm range. PDR models predict that these lines originate in the transition region between C^+ and CO (Tielens & Hollenbach 1985; Kaufman et al. 1999). However, several mechanisms, such as turbulent diffusion, non-chemical equilibrium, or intense X-ray radiation, can influence the C^0 distribution and abundance (Papadopoulos et al. 2004 and references therein).

To date, there are relatively few published SPIRE/FTS spectra of extragalactic objects (van der Werf et al. 2010; Panuzzo et al. 2010; Rangwala et al. 2011; Kamenetzky et al. 2012; Spinoglio et al. 2012; Meijerink et al. 2013); in these,

* *Herschel* is an ESA space observatory with science instruments provided by European-led Principal Investigator consortia and with important participation from NASA.

† Partly based on observations carried out with the IRAM 30 m Telescope. IRAM is supported by INSU/CNRS (France), MPG (Germany), and IGN (Spain).

Table 1
Sample of Local Active Galaxies

Galaxy	R.A. (J2000.0)	Decl. (J2000.0)	cz[a] (km s^{-1})	Dist.[b] (Mpc)	Spect. Class[c]	Ref.[d]	log L_{IR}[e] ($L_\odot$)	L_X[f] (10^{41} erg s^{-1})	Ref.[g]
NGC 1056	02 42 48.3	+28 34 27	1545	32.2	H II	1	10.3	...	...
UGC 05101	09 35 51.6	+61 21 11	11802	163	LINER	1	12.0	75	7
NGC 3227	10 23 30.6	+19 51 54	1157	14.4	Sy1.5	2	9.9	1.9	8
NGC 3982	11 56 28.1	+55 07 31	1109	20.6	Sy1.9	2	10.0	<0.025	9
NGC 4051	12 03 09.6	+44 31 53	700	14.6	Sy1.2	2	10.0	1.3	10
NGC 4151	12 10 32.6	+39 24 21	995	12.1	Sy1.5	2	9.8	8.2	10
NGC 4388	12 25 46.7	+12 39 44	2524	18.2	Sy1.9/HBLR	2, 3	10.2	3.0	11
IC 3639	12 40 52.8	−36 45 21	3275	42.5	Sy2/HBLR	1, 4	10.8	0.17	12
NGC 7130	21 48 19.5	−34 57 04	4842	66.0	Sy2	1	11.4	0.83	13
NGC 7172	22 02 01.9	−31 52 11	2603	33.9	Sy2	5	10.4	29	10
NGC 7582	23 18 23.5	−42 22 14	1575	20.6	H II/Sy1i	1, 6	10.8	2.0	14

Notes.
[a] Heliocentric velocity from NASA/IPAC extragalactic database (NED).
[b] Distance from NED.
[c] Nuclear activity classification. Sy1i indicates that broad emission lines are observed in the near-IR. HBLR indicates the detection of a hidden broad line region.
[d] Reference for the nuclear activity classification.
[e] 8–1000 μm infrared luminosity from Sanders et al. (2003) scaled to our adopted distance.
[f] X-ray 2–10 keV luminosity.
[g] Reference for the X-ray luminosity.
References. (1) Yuan et al. 2010; (2) Ho et al. 1997; (3) Young et al. 1996; (4) Heisler et al. 1997; (5) Lumsden et al. 2001; (6) Reunanen et al. 2003; (7) Imanishi et al. 2003; (8) Gondoin et al. 2003; (9) Guainazzi et al. 2005; (10) Brightman & Nandra 2011; (11) Cappi et al. 2006; (12) Guainazzi et al. 2005; (13) Levenson et al. 2005; (14) Piconcelli et al. 2007.

however, molecules such as H_2O, OH^+, and HF are often detected. In addition, other molecules like HCN, CH^+, and H_2O^+ have also been detected.

In this paper, we present for the first time the complete sub-mm spectra of a sample of 11 active galaxies (Section 2). The sub-mm spectra are complemented by ground-based IRAM 30 m observations of the CO $J = 1$–0 and $J = 2$–1 transitions in three galaxies. The SPIRE and IRAM 30 m observations and data reduction are described in Section 3. We use the escape probability approximation to model the CO and C^0 emission and study how they trace the warm and cold molecular gas in these galaxies (Sections 4 and 5). In two galaxies, we detect the HF $J = 1$–0 transition, one in emission and one in absorption. We discuss several possible origins for this line in Section 6. Finally, a brief discussion about the H_2O and OH^+ lines detected in a few galaxies is presented in Section 7. The [N II] line at 205 μm (1461 GHz) is one of the brightest far-IR lines in galaxies (e.g., Wright et al. 1991), however, it has not been systematically explored by previous observatories. In a forthcoming paper, we will study the emission of the [N II] 205 μm line and other far-IR atomic fine structure emission lines in our sample of galaxies. Throughout this paper, we assumed $H_0 = 73$ km s^{-1} Mpc^{-1}.

2. SAMPLE OF LOCAL ACTIVE GALAXIES

We study a sample of 11 local ($d = 12$–160 Mpc) active galaxies drawn from the 12 μm galaxy sample (Rush et al. 1993). They were selected because of their high *IRAS* 100 μm flux and to include the different nuclear activity classes in similar proportions (three Seyferts type 1.2 and 1.5, two type 1.9 Seyfert, three type 2 Seyfert, one low-ionization nuclear emission line region (LINER), and two H II galaxies). Their total infrared (IR) luminosities (L_{IR}) range from $10^{9.8}$ to $10^{12.0}$ $L_\odot$, and the median value is $10^{10.3}$ $L_\odot$. In our sample, only UGC 05101 and NGC 7130 are classified as luminous IR galaxies (LIRGs; $L_{IR} > 10^{11}$ $L_\odot$), so in these galaxies, besides the active galactic nucleus (AGN) activity, intense star formation is expected (Petric et al. 2011; Alonso-Herrero et al. 2012). The galaxies in our sample are presented in Table 1.

3. OBSERVATIONS AND DATA REDUCTION

All the galaxies in our sample were observed with the SPIRE/FTS and the SPIRE photometer on board *Herschel*. Additionally, we observed the CO $J = 1$–0 and $J = 2$–1 rotational transitions in UGC 05101, NGC 3227, and NGC 3982 with the IRAM 30 m telescope. The SPIRE photometric data will be analyzed in detail in a forthcoming paper, but the data reduction is summarized here because the images are used to calculate the source–beam coupling factor and the scaling factor for the flux calibration of the SPIRE/FTS spectra.

3.1. SPIRE/FTS Spectroscopy

We collected *Herschel* SPIRE/FTS spectroscopic observations of 11 nearby active galaxies through a guaranteed time project (PI: L. Spinoglio) and a guaranteed time key project (PI: C. D. Wilson). The integration times of the observations were ∼5100 s, achieving a sensitivity of 0.2–0.3 Jy in the continuum and a 3σ detection limit of $\sim 1 \times 10^{-14}$ erg cm^{-2} s^{-1} for an unresolved spectral line.

The SPIRE/FTS has two bolometer arrays: the spectrometer short wavelength (SSW; 194–324 μm and 925–1545 GHz) and the spectrometer long wavelength (SLW; 316–672 μm and 446–948 GHz). The beam full width at half-maximum (FWHM) of the SSW bolometers is ∼18″, approximately constant with frequency. On the contrary, the beam FWHM of the SLW bolometers varies between ∼30″ and ∼42″ with a complicated dependence on frequency (Swinyard et al. 2010). At the distances of our galaxies, 30″ corresponds to physical scales of 2–20 kpc. They sparsely sample a field of view (FOV) of ∼2′, with the central bolometer of the arrays centered at the nuclei of the galaxies (see Figure 1).

All the galaxies were observed at high spectral resolution (unresolved line FWHM 1.45 GHz and $\nu/\Delta\nu \sim$ 300–1000)

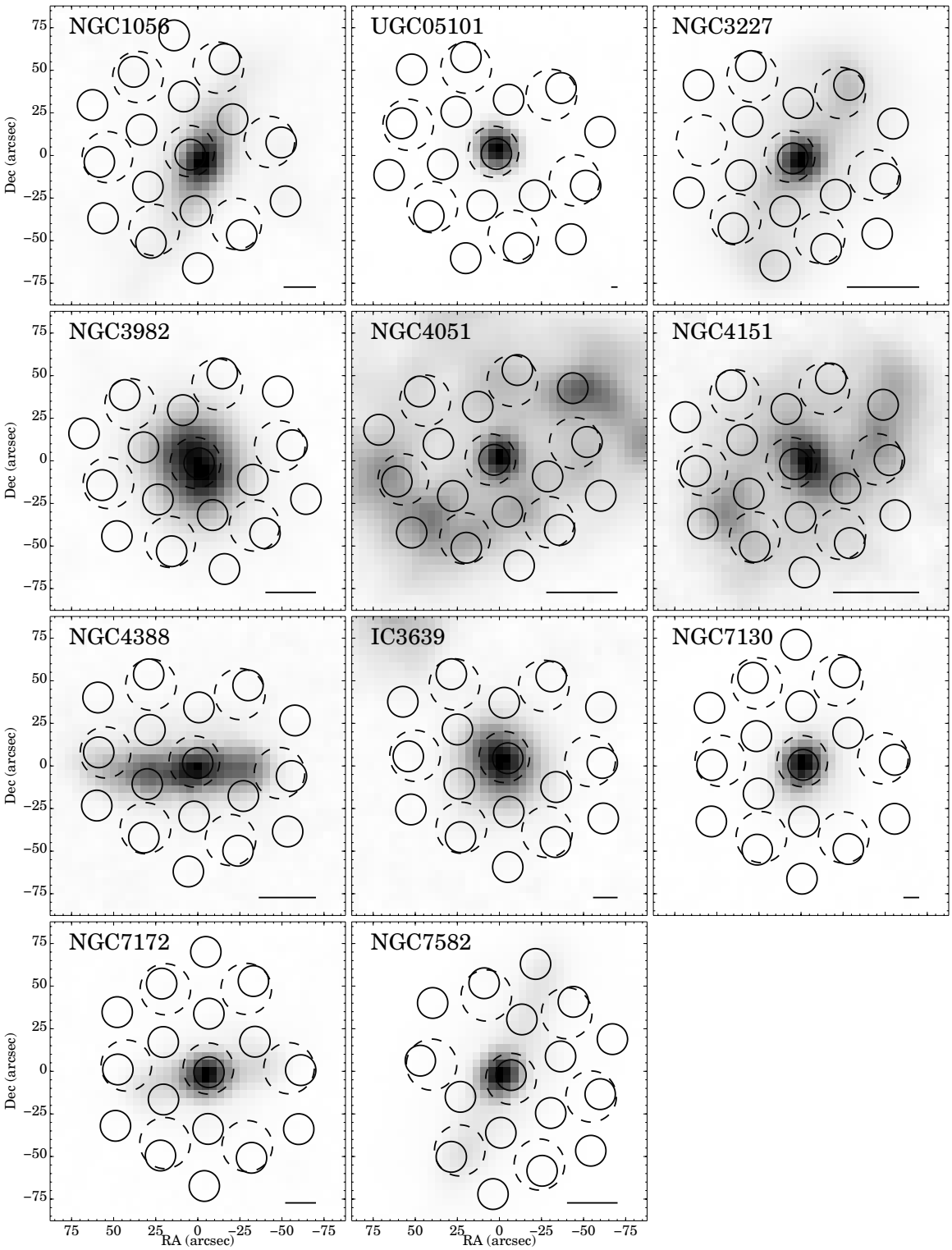

Figure 1. Footprint of SPIRE/FTS FOV plotted over the *Herschel*/SPIRE 250 μm images of our sample of Seyfert galaxies. The solid and dashed circles mark the positions of the SSW and SLW bolometers, respectively. Only the functioning detectors in the unvignetted FOV are plotted. North is up and east is to the left. The images are shown in a linear gray scale. The black line represents 3 kpc at the distance of the galaxy.

in the single pointing mode. The observation IDs are listed in Table 2.

We processed the raw data with the Herschel interactive pipeline environment software (HIPE) version 9 (Ott 2010). We used the standard reduction scripts (Fulton et al. 2010). These scripts process the raw SPIRE/FTS timelines and produce a flux calibrated spectrum for each bolometer. Briefly, first the bolometer timelines are corrected for instrumental effects and cosmic-ray hits, and the interferograms are created. The baselines are removed and the phase of the interferograms corrected before a Fourier transform is applied to obtain the spectra. These spectra are dominated by the telescope (and instrument) thermal emission that must be removed to obtain the source spectrum.

Table 2
Log of *Herschel* Observations

Galaxy	SPIRE/FTS Spectrometer Observation ID	SPIRE Photometer Observation ID
NGC 1056	1342204024	1342226630
UGC 05101	1342209278	1342204962
NGC 3227	1342209281	1342197318
NGC 3982	1342209277	1342186862
NGC 4051	1342209276	1342210502
NGC 4151	1342209852	1342188588
NGC 4388	1342210849	1342211416
IC 3639	1342213381	1342202200
NGC 7130	1342219565	1342210527
NGC 7172	1342219549	1342209301
NGC 7582	1342209280	1342210529

The uncertainty in the telescope emission model used by HIPE is 1–2 Jy in the continuum level (SPIRE Observer's Manual[10]), which is comparable to the fluxes of our galaxies. Therefore, the residual telescope emission has to be subtracted before applying the point source correction to the spectra. The optical angular sizes of our galaxies are several arcminutes (UGC 05101 and NGC 7130 are almost point-like at the SPIRE/FTS angular resolution, see Figure 1), but the nuclear far-IR emission is approximately point-like at the angular resolution of SPIRE. Moreover, far-IR emission is detected only in the central bolometer of the SPIRE/FTS arrays (FWHM $\sim$ 18″ and 30–40″ for the SSW and SLW arrays, respectively). Thus, we estimated the residual telescope emission averaging the spectra of the off-axis bolometers. For some galaxies, some of the off-axis detectors contain extended galactic emission (weak continuum and [N II]1461 GHz emission). We excluded those detectors before averaging.

Next, we applied the point source correction[11] to the central bolometer spectra to obtain the flux calibrated spectra of the galactic nuclei. To correct for the large beam size variations in the SLW spectra, we calculated the source–beam coupling factor, η. We define η as the ratio between the flux measured with a beam of size θ and that measured with a 30″ beam (the minimum SLW beam size). Similar to Kamenetzky et al. (2012) and Panuzzo et al. (2010), we convolved the 250 μm SPIRE maps using Gaussian profiles to obtain the coupling factor as a function of the beam size, $\eta(\theta)$. Then, with the SLW beam size dependence on the frequency[11], $\theta(\nu)$, we obtained $\eta(\nu)$ and we divided the SLW spectra by this function. The values of $\eta(\nu)$ for these galaxies vary between 1.0 and 1.4. By applying this correction, we assume that the spatial distributions of the emission lines in the SPIRE/FTS spectra are comparable to that of the cold dust traced by the 250 μm emission.

Finally, we scaled the SSW and SLW spectra to match the SPIRE photometry (see Section 3.2). For the SSW, we scaled the spectra to match the 250 μm (1200 GHz) flux measured in a 18″ diameter aperture. Similarly, we scaled the SLW spectra to match the flux measured in the 350 μm (856 GHz) image in a 30″ diameter aperture. We used the 350 μm SPIRE image because for most of our sources, the continuum at 500 μm (600 GHz) is below the detection limit of the FTS data. Point source aperture corrections are applied to the SPIRE photometry (see Section 3.2). The scale factors vary between 0.85 and 1.30 for the SSW spectra and between 0.95 and 1.20 for the SLW spectra. For NGC 1056, NGC 4051, NGC 4151, IC 3639, and NGC 7172, the 350 μm continuum is not detected in the FTS spectra. Thus, for these galaxies, the uncertainty in the absolute flux of the emission lines in the SLW range is about 20% larger. The final flux calibrated spectra of the galaxies are shown in Figure 2.

We measured the line intensities by fitting a sinc profile[12] to the emission lines. To obtain the local continuum, we used a linear fit in a $\sim$10 GHz range around the line position. When two lines were close in frequency (e.g., CO J = 7–6 at 807 GHz and [C I]809 GHz), the two lines were fitted simultaneously. In the SPIRE/FTS spectra of our galaxies, we find CO lines from J_{up} = 4 to J_{up} = 12, the [C I]492 GHz, [C I]809 GHz, and [N II]1461 GHz atomic lines, and some water lines. The HF J = 1–0 rotational transition at 1232 GHz is detected in two sources and in one source we detect three OH^+ transitions. The fluxes and 1σ uncertainties of the detected lines and the 3σ upper limits for the undetected lines are given in Tables 3 and 4.

3.2. SPIRE Photometry

We obtained *Herschel* SPIRE imaging observations for seven of our galaxies through a guaranteed time project (PI: L. Spinoglio). The rest of the galaxies in our sample were observed as part of the Very Nearby Galaxies Survey (PI: C. D. Wilson) and the Herschel Reference Survey (PI: S. Eales) programs and the data were available in the *Herschel* archive. The SPIRE photometer consists of three bolometer arrays that observe in three spectral bands centered at 250, 350, and 500 μm. Depending on the angular size of the galaxies, they were observed in the small or in the large scan-map mode in the three bands. At least two scans in perpendicular directions were performed for each galaxy.

First, we processed the raw data using HIPE version 9 to create the flux calibrated timelines for each bolometer. The standard HIPE pipeline corrects for instrumental effects and attaches the pointing information to the timelines. Then, the timelines were combined to create the maps using Scanamorphos version 18 (Roussel 2012). Scanamorphos detects and masks glitches in the data, performs the baseline subtraction, and projects the timelines in a spatial grid.

To measure the nuclear fluxes of the galaxies, we first converted the maps produced by Scanamorphos in Jy beam^{-1} to Jy arcsec^{-1}. We adopted the beam areas given by the SPIRE Observer's Manual (423, 751, and 1587 arcsec^2 for the 250, 350, and 500 μm bands, respectively). Then, we performed aperture photometry using an aperture of diameter 18″ in the 250 μm image and 30″ in the 350 and 500 μm maps and we multiplied the measured fluxes by an aperture correction. The values of these corrections are 2.33, 1.75, and 3.02 for the 250, 350, and 500 μm fluxes, respectively. These aperture correction factors were calculated from a map of Neptune processed following the same reduction steps described above. We did not apply any color correction to the fluxes because this correction is expected to be small, <5 %, for blackbody emission (SPIRE Observer's Manual). The measured fluxes are presented in Table 5.

For most of these galaxies, the nuclear region is only marginally resolved at the angular resolution of SPIRE (18″, 25″, and 37″ for the 250, 350, and 500 μm bands, respectively).

[10] Available at http://herschel.esac.esa.int/Docs/SPIRE/html/spire_om.html.
[11] Taken from the HIPE version 9 calibration product `BeamParam_HR_unapod_nominal_20050222`. It provides the point source correction and the beam size as a function of frequency with a 0.3 GHz sampling.
[12] The sinc function represents well the SPIRE/FTS instrumental line shape (see the SPIRE Observer's Manual).

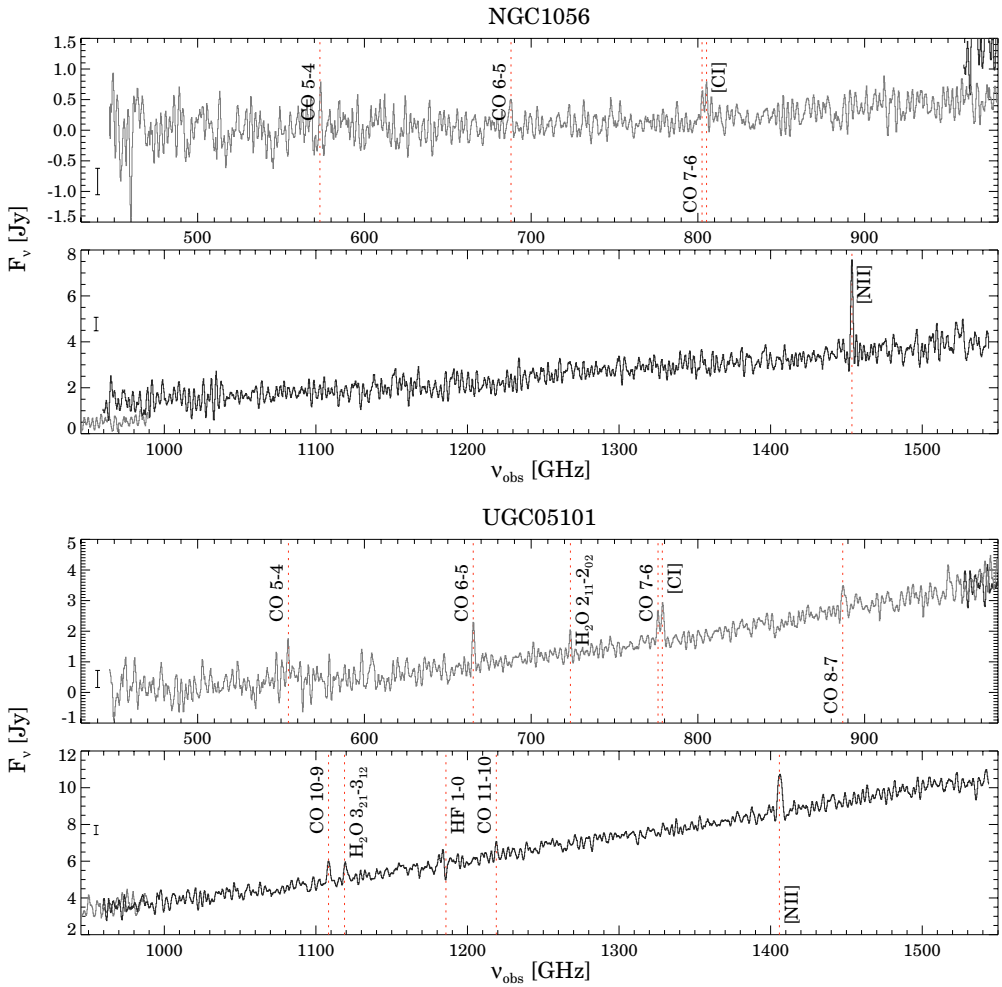

Figure 2. Observed SPIRE/FTS spectra of our sample. The black and gray lines are the SSW and SLW spectra, respectively. Note the overlap between the two spectra in the 960 and 990 GHz spectral range. The dashed red lines mark the position of the detected lines. The error bars indicate the median 1σ uncertainty of each spectrum.

(A color version of this figure is available in the online journal.)

However, for NGC 4051 and NGC 4151, the nuclear emission is more extended, so the reported flux for these two galaxies might be overestimated due to the aperture correction applied. For the two more distant galaxies in our sample, UGC 05101 and NGC 7130, the fluxes in Table 5 correspond to the galaxy integrated sub-mm emission, since they are point sources in the SPIRE images. For the rest, the fluxes should be considered a lower limit to their total sub-mm emission.

3.3. Ground-based CO Observations

We performed pointed observations of low-J CO lines in three galaxies, UGC 05101, NGC 3227, and NGC 3982. The observations were conducted from 2011 October 1 to October 3 with the IRAM 30 m telescope on Pico Veleta (Spain). We used the heterodyne eight mixer receiver (EMIR) using different frequency setups, depending on the target. For NGC 3227 and NGC 3982, we used two frequency setups, one centered at 98.875 GHz for the 3 mm band (E0) to encompass the emission of CO $J = 1$–0 and ^{13}CO $J = 1$–0, and another one that combines the 3 mm band (E0) and 1 mm band (E2), centered at 89.375 GHz and 230.538 GHz, respectively, to cover the emission of the CO $J = 2$–1 line. For UGC 05101, the receiver was tuned at 98.875 GHz and 230.538 GHz to cover the CO $J = 1$–0 and CO $J = 2$–1 lines. The ^{13}CO $J = 1$–0 was outside the observed bands for UGC 05101. The 16 GHz bandwidth of the EMIR receivers were connected to the 195 kHz resolution FTSs, providing a channel-width spacing of ∼0.6 km s^{-1} for the 3 mm band and ∼0.3 km s^{-1} for the 1 mm band, and to the wideband line multiple autocorrelator that provides a resolution of 2 MHz (5.2–6.7 km s^{-1} for the 3 mm band and ∼2.6 km s^{-1} at 230.538 GHz). The half-power beamwidth is 21.″3 at 115 GHz and 10.″7 at 230 GHz. Observations were performed in wobbler switching mode, with a throw of 120″. Weather conditions were good, with zenith optical depths between 0.1 and 0.3. System temperatures ranged from 100 K to 200 K in the 3 mm band and from 250 K to 800 K in the 1 mm band. Pointing was checked every two hours and the rms pointing error was 4″ at 3 mm. Focus was checked at the beginning of each run and during sunrise.

The data were reduced using the continuum and line analysis single-dish Software (CLASS) package of the Grenoble image and line data analysis software (GILDAS).[13] The observed spectra were converted from antenna temperature units (T_a^*) to main beam temperatures (T_{mb}) using the relation $T_{mb} = T_a^* \times (F_{eff}/B_{eff})$, where F_{eff} is the forward efficiency of the telescope ($F_{eff} = 0.95$ for the 3 mm band and $F_{eff} = 0.92$ for the

[13] http://www.iram.fr/IRAMFR/GILDAS

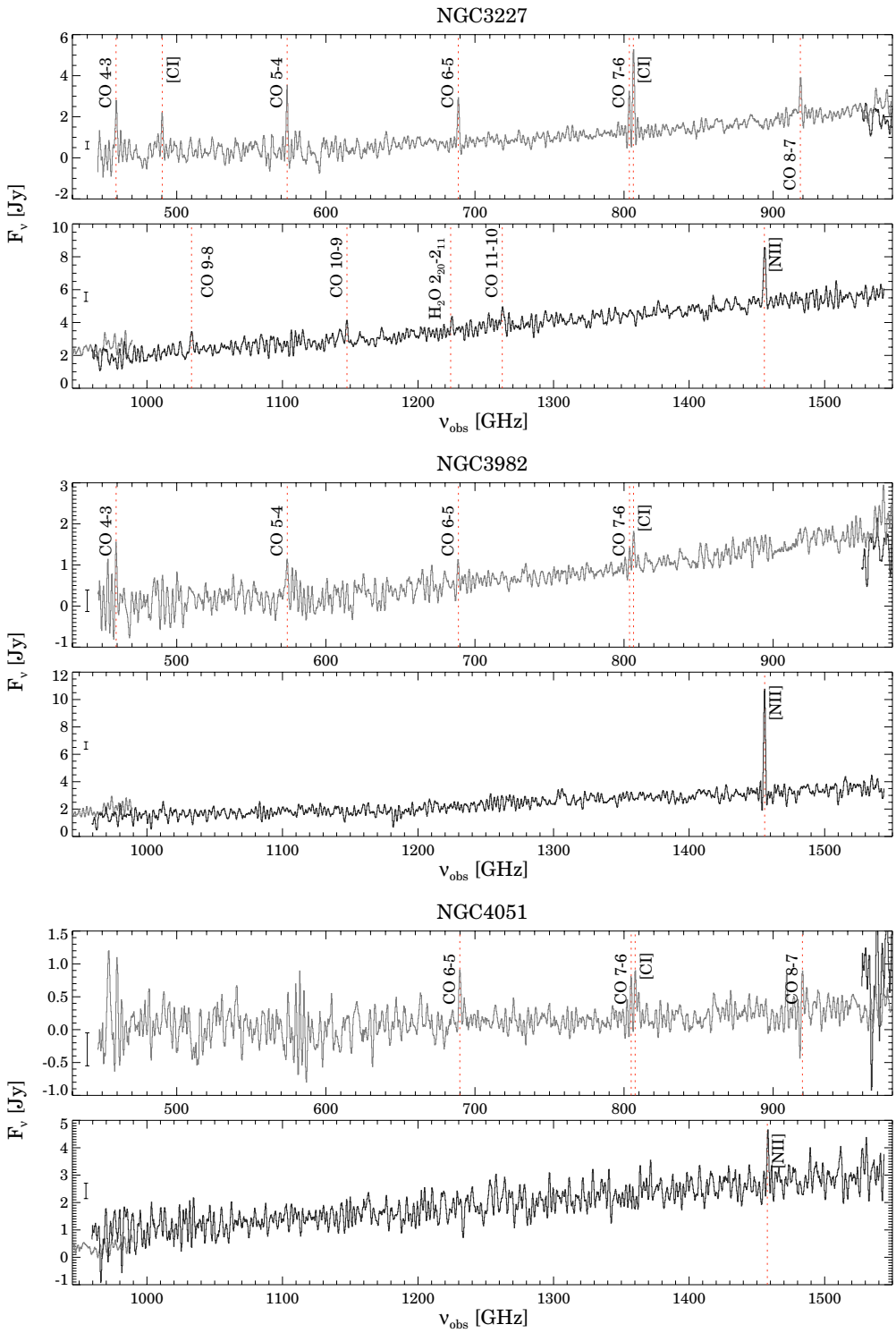

Figure 2. (Continued)

1 mm band) and $B_{\rm eff}$ is the main beam efficiency, ranging from 0.77 to 0.81 at 3 mm, and $B_{\rm eff} = 0.59$ at 1 mm. A second-order baseline was removed for each individual scan and co-added after inspection. The final spectra were smoothed to a common velocity resolution of 20 km s^{-1}. In this work, we present the results of the CO and ^{13}CO lines. The other molecular species detected within the EMIR bands will be presented and analyzed in a forthcoming paper.

In addition, we analyzed the CO $J = 3$–2 transition observed with the 15 m James Clerk Maxwell Telescope (JCMT) on Mauna Kea (USA) and the 10 m Heinrich Hertz Telescope (HHT) on Mt. Graham (USA) for these galaxies. These observations are described in detail by Wilson et al. (2008), Iono et al. (2009), and Mao et al. (2010).

3.3.1. CO Line Profile Fitting

The observed low-J CO transitions have broad and complex line profiles, suggesting that the CO emission is produced in several regions unresolved within the telescope beam. To estimate

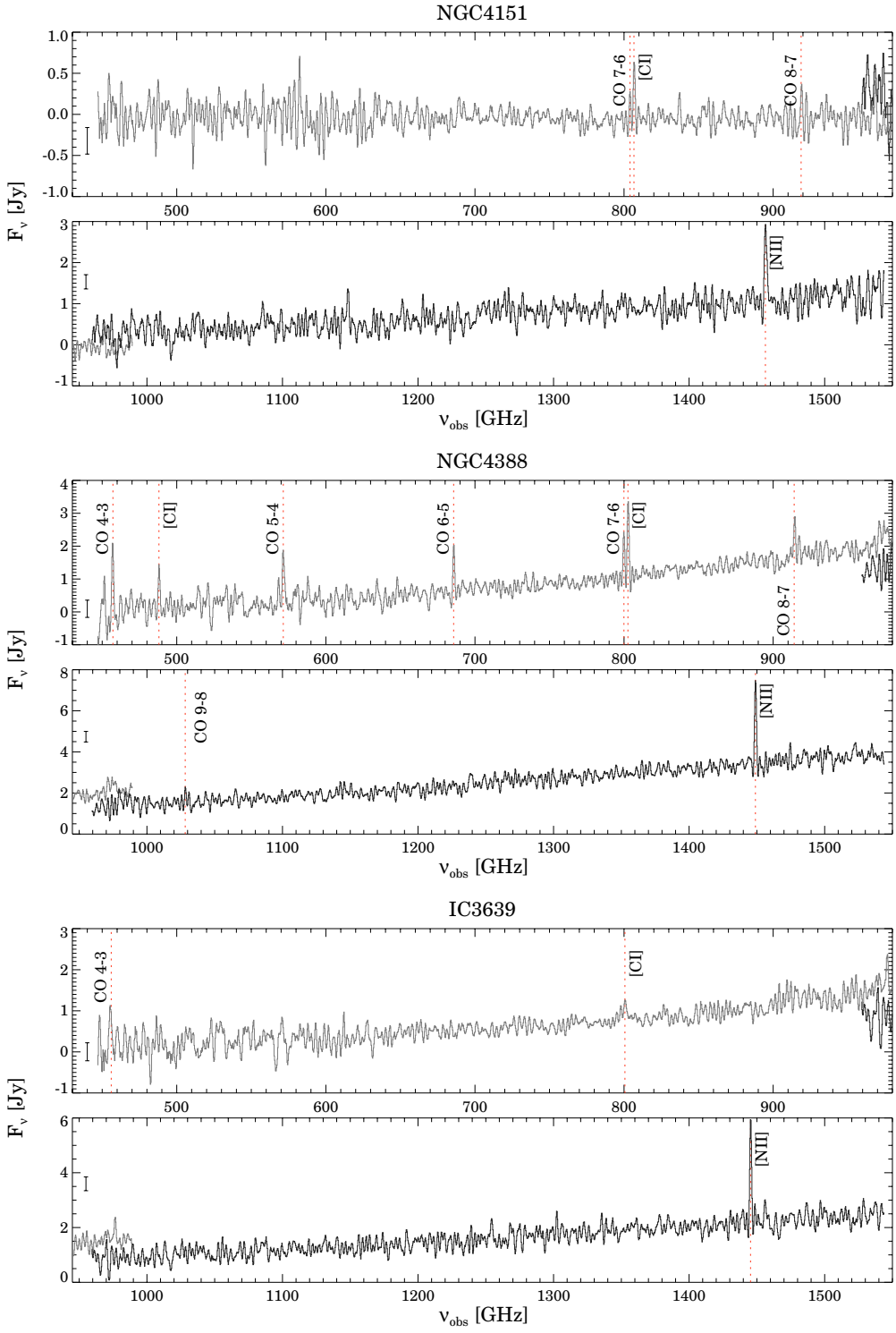

Figure 2. (Continued)

the CO intensity arising from each region, we fitted multiple Gaussians to the observed line profiles. Three Gaussians reproduce well the observed profiles in these galaxies.

First, we derived the FWHM and relative velocity of each kinematical component by fitting simultaneously the high signal-to-noise ratio (S/N) CO J = 1–0 and CO J = 2–1 line profiles. We assumed that the FWHM and relative velocity of each kinematical component are equal for both transitions, and only the peak intensities were allowed to vary. Then, to model the lower S/N ratio CO J = 3–2 and ^{13}CO J = 1–0 lines, we used the FWHM and velocity values derived before and fitted the peak intensities of each component. The best-fit models are shown in Figures 3–5. In Table 6, we show the results of the Gaussian fits.

3.3.2. Literature CO Data

We obtained from the literature the observed intensities of the CO J = 1–0, CO J = 2–1, and CO J = 3–2 transitions for the remaining galaxies (see Table 7). For most of them, the CO J = 1–0 and CO J = 2–1 intensities are available.

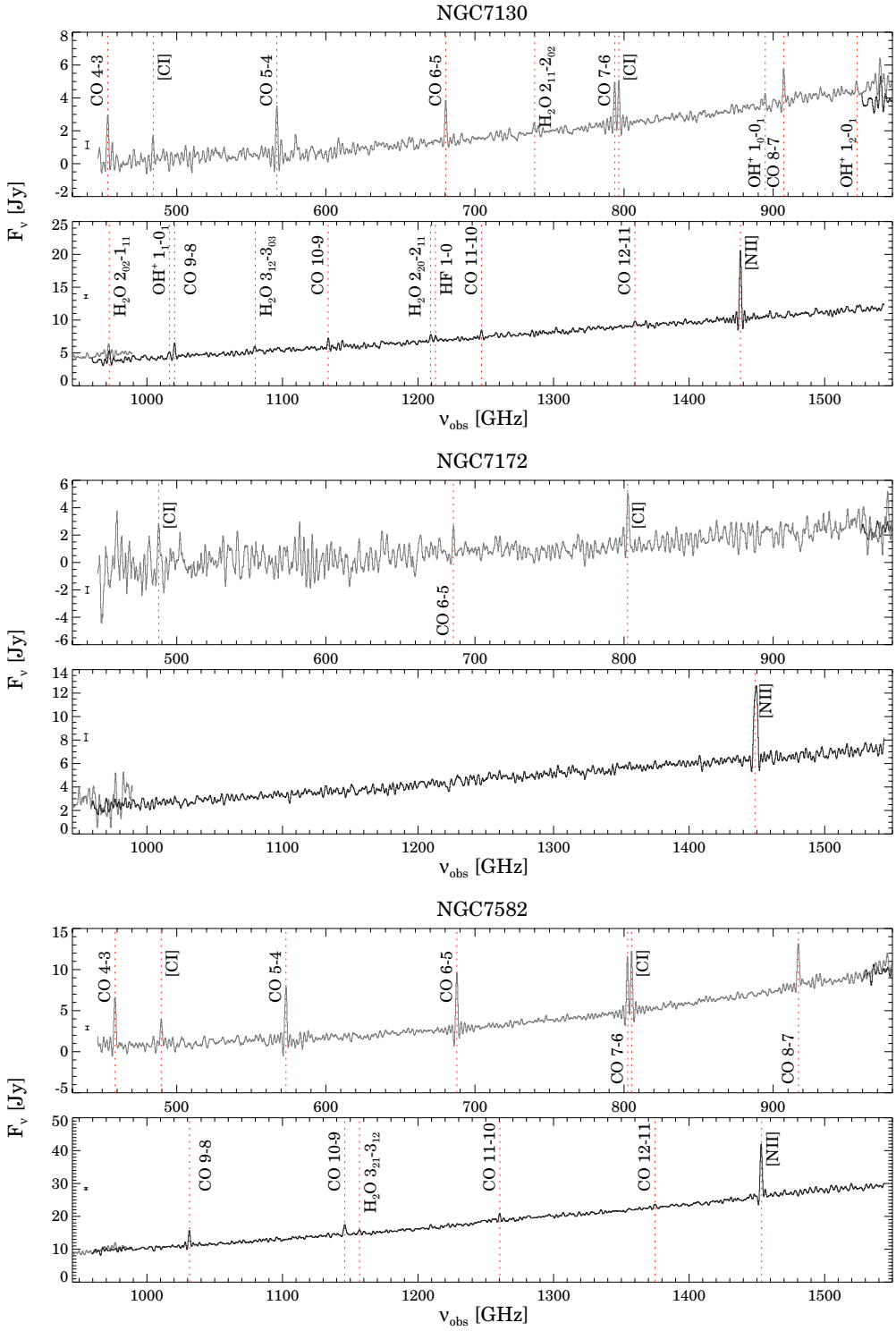

Figure 2. (Continued)

However, the CO $J = 3$–2 transition was observed in just three of them (see also Section 3.3.1).

For the three galaxies analyzed in Section 3.3.1, in Table 7, we list the CO fluxes corresponding to the component with the central recessional velocity. We associate this component with the compact nuclear CO emission, while the other two components are likely due to the rotation of the galaxy disk. The disk emission also contributes to the central component, so the adopted nuclear flux might be slightly overestimated.

4. CO EMISSION MODELING

In this section, we describe the analysis of the CO SLEDs of six of our galaxies with more than three CO lines detected in their SPIRE/FTS spectra. First, we describe the radiative transfer models used to interpret the CO SLEDs. The models for individual sources are discussed later. Finally, we derive the properties of the cold and warm molecular gas traced by the CO lines.

Table 3
SPIRE/FTS Line Fluxes

Transition	ν_{rest}	Fluxes (10^{-15} erg cm^{-2} s^{-1})					
	(GHz)	NGC 1056	UGC 05101	NGC 3227	NGC 3982	NGC 4051	NGC 4151
^{12}CO $J = 4$–3	461.041	<15.8	... [a]	29.0 ± 3.7	18.1 ± 2.7	<13.0	<9.5
^{12}CO $J = 5$–4	576.268	10.1 ± 2.0	15.6 ± 3.8	33.4 ± 3.9	12.9 ± 2.2	<11.2	<8.0
^{12}CO $J = 6$–5	691.473	6.0 ± 1.5	16.9 ± 2.3	25.2 ± 2.9	7.3 ± 1.6	9.6 ± 1.6	<4.1
^{12}CO $J = 7$–6	806.652	6.1 ± 1.4	11.1 ± 1.8	18.1 ± 2.3	4.7 ± 1.3	7.3 ± 1.4	3.6 ± 1.1
^{12}CO $J = 8$–7	921.800	<8.0	11.6 ± 2.6	23.7 ± 2.9	<10.1	7.6 ± 1.6	5.3 ± 1.3
^{12}CO $J = 9$–8	1036.912	<13.6	<11.7	14.6 ± 2.3	<12.1	<15.1	<8.1
^{12}CO $J = 10$–9	1151.985	<13.3	13.1 ± 2.5	15.7 ± 2.4	<12.9	<12.2	<9.8
^{12}CO $J = 11$–10	1267.015	<11.6	9.7 ± 2.9	13.9 ± 2.4	<13.6	<17.8	<9.0
^{12}CO $J = 12$–11	1381.995	<12.1	<8.7	<14.2	<13.0	<15.0	<9.0
^{12}CO $J = 13$–12	1496.923	<16.7	<11.5	<14.4	<15.6	<19.7	<11.4
p-H_2O 2_{11}–2_{02}	752.033	<5.8	8.5 ± 1.8	<7.5	<5.3	<5.3	<3.1
p-H_2O 2_{02}–1_{11}	987.927	<18.2	<11.0	<14.4	<15.3	<20.7	<10.9
o-H_2O 3_{12}–3_{03}	1097.365	<11.6	<9.6	<12.9	<11.0	<12.2	<8.1
p-H_2O 1_{11}–0_{00}	1113.343	<13.0	<11.4	<13.7	<10.6	<12.2	<8.4
o-H_2O 3_{21}–3_{12}	1162.912	<14.1	10.8 ± 2.4	<11.2	<12.0	<12.3	<10.2
p-H_2O 2_{20}–2_{11}	1228.789	<11.9	<12.9	12.0 ± 3.2	<11.2	<16.4	<9.5
[C I] $^3P_1$–$^3P_0$	492.161	<12.2	<16.0	22.7 ± 4.3	<13.2	<11.3	<6.9
[C I] $^3P_2$–$^3P_1$	809.342	7.7 ± 1.5	15.8 ± 2.1	46.6 ± 1.9	10.0 ± 1.5	7.8 ± 1.3	8.4 ± 1.0
[N II] $^3P_1$–$^3P_0$	1461.128	50.5 ± 3.4	37.9 ± 4.4	38.6 ± 4.3	88.1 ± 3.7	25.0 ± 4.3	21.2 ± 3.1

Transition	ν_{rest}	Fluxes (10^{-15} erg cm^{-2} s^{-1})				
	(GHz)	NGC 4388	IC 3639	NGC 7130	NGC 7172	NGC 7582
^{12}CO $J = 4$–3	461.041	23.9 ± 2.9	12.1 ± 1.9	35.3 ± 3.9	<53.9	69.3 ± 7.2
^{12}CO $J = 5$–4	576.268	19.1 ± 2.4	<10.3	36.6 ± 3.9	<43.7	78.0 ± 8.0
^{12}CO $J = 6$–5	691.473	15.4 ± 1.9	<5.4	27.7 ± 3.0	21.2 ± 2.8	82.3 ± 8.3
^{12}CO $J = 7$–6	806.652	13.1 ± 1.7	<4.8	27.8 ± 2.9	<19.0	65.6 ± 6.7
^{12}CO $J = 8$–7	921.800	14.1 ± 1.8	<7.3	22.2 ± 2.6	<27.9	63.1 ± 6.5
^{12}CO $J = 9$–8	1036.912	9.7 ± 1.6	<9.6	25.2 ± 2.8	<9.3	54.6 ± 5.7
^{12}CO $J = 10$–9	1151.985	<8.1	<9.2	18.8 ± 2.4	<10.4	35.1 ± 3.8
^{12}CO $J = 11$–10	1267.015	<10.8	<11.2	12.9 ± 1.8	<12.3	26.4 ± 3.0
^{12}CO $J = 12$–11	1381.995	<8.0	<8.6	10.3 ± 1.6	<9.3	10.9 ± 1.9
^{12}CO $J = 13$–12	1496.923	<12.2	<11.4	<12.4	<11.9	<22.4
p-H_2O 2_{11}–2_{02}	752.033	<5.8	<4.6	6.6 ± 0.9	<18.1	<9.2
p-H_2O 2_{02}–1_{11}	987.927	<11.0	<11.7	18.6 ± 2.0	<12.1	<16.9
o-H_2O 3_{12}–3_{03}	1097.365	<8.1	<9.6	12.2 ± 1.5	<9.0	<14.0
p-H_2O 1_{11}–0_{00}	1113.343	<8.3	<8.8	<9.5	<9.6	<11.8
o-H_2O 3_{21}–3_{12}	1162.912	<16.7	<8.2	<12.8	<18.7	13.9 ± 2.1
p-H_2O 2_{20}–2_{11}	1228.789	<11.0	<10.0	12.8 ± 1.1	<9.9	<13.1
[C I] $^3P_1$–$^3P_0$	492.161	14.5 ± 2.0	<11.7	17.9 ± 2.2	38.2 ± 5.2	34.4 ± 2.8
[C I] $^3P_2$–$^3P_1$	809.342	26.7 ± 0.7	5.8 ± 0.7	28.2 ± 1.0	45.0 ± 4.0	75.9 ± 2.0
[N II] $^3P_1$–$^3P_0$	1461.128	47.4 ± 1.9	45.5 ± 2.1	123.0 ± 1.8	120.1 ± 4.1	191.8 ± 5.4

Notes. Measured line fluxes and 1σ statistical uncertainties. For the non-detections, we state the 3σ upper limits.
[a] Due to the higher redshift of UGC 05101, the CO $J = 4$–3 transition is outside the SPIRE/FTS range.

Table 4
SPIRE/FTS HF and OH^+ Fluxes

Galaxy	Transition	ν_{rest} (GHz)	Flux (10^{-15} erg cm^{-2} s^{-1})
UGC 05101	HF $J = 1$–0	1232.476	−10.4 ± 2.3
NGC 7130	HF $J = 1$–0	1232.476	8.6 ± 1.1
	OH^+ 1_0–0_1	909.159	7.6 ± 1.2
	OH^+ 1_2–0_1	971.805	9.6 ± 2.4
	OH^+ 1_1–0_1	1033.118	11.2 ± 1.5

Notes. Fluxes and 1σ statistical uncertainties for the HF and OH^+ detections.

4.1. Radiative Transfer Models

We used the non-local thermodynamic equilibrium radiative transfer code RADEX (van der Tak et al. 2007) to infer the physical conditions in the regions where the mid-J CO emission is produced. RADEX uses the escape probability approximation to solve iteratively for the molecular level populations and the intensities of the CO lines.

We produced a grid of models assuming a spherically symmetric homogeneous medium. These models span a wide range in kinetic temperature (T_{kin} = 50–3000 K), molecular hydrogen density (n_{H_2} = 10–10^5 cm^{-3}), and CO column density per unit of line width ($N_{CO}/\Delta v = 10^{12} - 10^{17}$ cm^{-2}/km s^{-1}). We adopted the collisional rate coefficients between CO and H_2 of Yang et al. (2010). For the background radiation, we used the cosmic microwave background at 2.73 K, the inclusion of the local far-IR background does not significantly modify the models (see Spinoglio et al. 2012).

The CO lines are spectroscopically unresolved in the FTS spectra of these galaxies, so we used ground-based observations

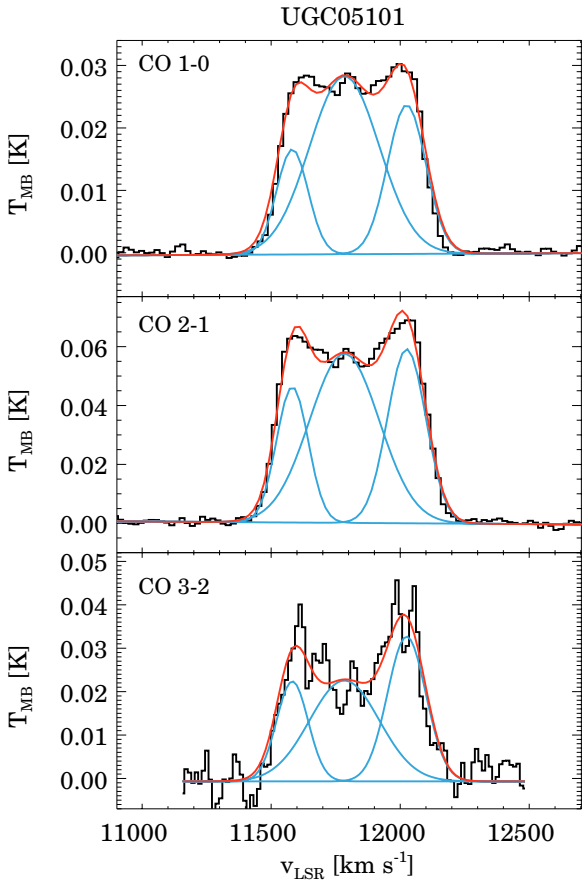

Figure 3. Observed line profiles and best-fit models of the CO $J = 1$–0 and CO $J = 2$–1 transitions observed with IRAM 30 m and the CO $J = 3$–2 transition observed with JCMT 15 m for UGC 05101. The spectra are smoothed to a velocity resolution of 20 km s^{-1}. The narrower spectral coverage of the CO $J = 3$–2 transition is due to the narrower instantaneous bandwidth of the JCMT receivers.

(A color version of this figure is available in the online journal.)

Table 5
SPIRE Photometry

Galaxy	$F_\nu(250\ \mu m)$ (Jy)	$F_\nu(350\ \mu m)$ (Jy)	$F_\nu(500\ \mu m)$ (Jy)
NGC 1056	2.15 ± 0.03	1.09 ± 0.02	0.439 ± 0.012
UGC 05101	5.83 ± 0.11	2.35 ± 0.04	0.785 ± 0.019
NGC 3227	3.14 ± 0.02	1.55 ± 0.01	0.611 ± 0.005
NGC 3982	1.89 ± 0.01	1.24 ± 0.01	0.566 ± 0.009
NGC 4051	1.49 ± 0.02	0.780 ± 0.011	0.343 ± 0.011
NGC 4151	0.592 ± 0.007	0.305 ± 0.005	0.133 ± 0.008
NGC 4388	2.39 ± 0.07	1.33 ± 0.03	0.614 ± 0.019
IC 3639	1.56 ± 0.02	0.845 ± 0.011	0.392 ± 0.012
NGC 7130	6.49 ± 0.10	2.92 ± 0.04	1.04 ± 0.02
NGC 7172	4.14 ± 0.06	1.84 ± 0.03	0.711 ± 0.015
NGC 7582	16.2 ± 0.3	6.47 ± 0.09	2.26 ± 0.04

Notes. Nuclear fluxes measured in the SPIRE 250, 350, and 500 μm images. The aperture size is 18″ for the 250 μm flux and 30″ for the 350 and 500 μm fluxes. Aperture corrections have been applied (see Section 3.2).

of the low-J CO lines to determine the value of Δv (see Section 4.2 for details).

The free parameters of the models are $T_{\rm kin}$, $n_{\rm H_2}$, $N_{\rm CO}$, and the filling factor Φ. The filling factor represents the fraction of the beam area occupied by the source. When the emission is optically thin ($\tau \ll 1$), in the escape probability approximation, the line ratios only depend on $T_{\rm kin}$ and $n_{\rm H_2}$, whereas the absolute

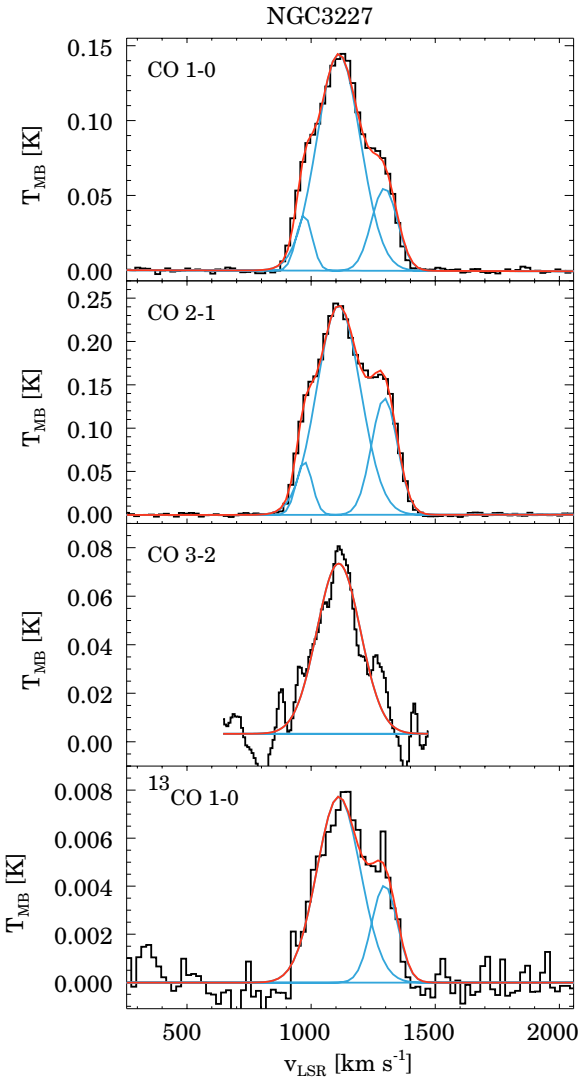

Figure 4. Same as Figure 3, but for NGC 3227. For this galaxy, the CO $J = 3$–2 transition was observed with the HHT 10 m. The narrower spectral coverage of the CO $J = 3$–2 transition is due to the narrower instantaneous bandwidth of the HHT receivers.

(A color version of this figure is available in the online journal.)

fluxes depend on the $N_{\rm CO}\Phi$ product. Consequently, it is not possible to determine simultaneously $N_{\rm CO}$ and the filling factor, and since the size of the CO emitting region (i.e., the filling factor) in our galaxies is not accurately known, we can only estimate the beam-averaged column density, $\langle N_{\rm CO}\rangle = N_{\rm CO}\Phi$.

We estimated the values and uncertainties on the model parameters using a Monte Carlo method. From the fluxes and their associated uncertainties listed in Tables 3 and 7, we constructed 500 CO SLED simulations for each galaxy that were fitted using a χ^2 minimization algorithm. The parameter values and 1σ uncertainties reported in Table 8 are those obtained from the parameter distributions in the Monte Carlo simulations. The best-fit models of the six analyzed galaxies are shown in Figure 6.

From the derived column densities, we calculated the molecular gas masses using the following expression:

$$M_{\rm mol} = \mu \langle N_{\rm CO}\rangle {x_{\rm CO}}^{-1} \Omega d^2 m_{\rm H_2}, \quad (1)$$

where $\mu = 1.4$ is the mean molecular weight per H atom, $\langle N_{\rm CO}\rangle$ is the beam-averaged CO column density, $x_{\rm CO} = 3 \times 10^{-4}$ is the

Table 6
CO Line Profile Fitting Results

Galaxy	v_{LSR}[a] (km s^{-1})	FWHM (km s^{-1})	CO J = 1–0 (K km s^{-1})	CO J = 2–1 (K km s^{-1})	CO J = 3–2 (K km s^{-1})	^{13}CO J = 1–0 (K km s^{-1})
UGC 05101	11784	318 ± 32	9.64 ± 0.38	19.46 ± 0.64	7.9 ± 1.6	···
	11581	144 ± 8	2.58 ± 0.17	7.07 ± 0.29	3.53 ± 0.72	···
	12025	175 ± 5	4.45 ± 0.21	11.04 ± 0.35	6.22 ± 0.87	···
NGC 3227	1110	206 ± 8	31.83 ± 0.45	53.17 ± 0.53	15.4 ± 2.0	1.70 ± 0.15
	972	75 ± 7	2.97 ± 0.16	4.92 ± 0.19	<2.2	<0.2
	1295	122 ± 4	7.21 ± 0.27	17.60 ± 0.31	<3.6	0.53 ± 0.09
NGC 3982	1114	102 ± 9	7.31 ± 0.26	8.53 ± 0.33	4.3 ± 1.4	0.70 ± 0.10
	1061	46 ± 5	3.25 ± 0.12	4.20 ± 0.15	<1.8	0.28 ± 0.05
	1189	45 ± 8	1.87 ± 0.12	<0.5	4.94 ± 0.61	0.14 ± 0.05

Note. [a] The uncertainties of the measured radio local standard of rest (LSR) velocities are ∼30 km s^{-1}.

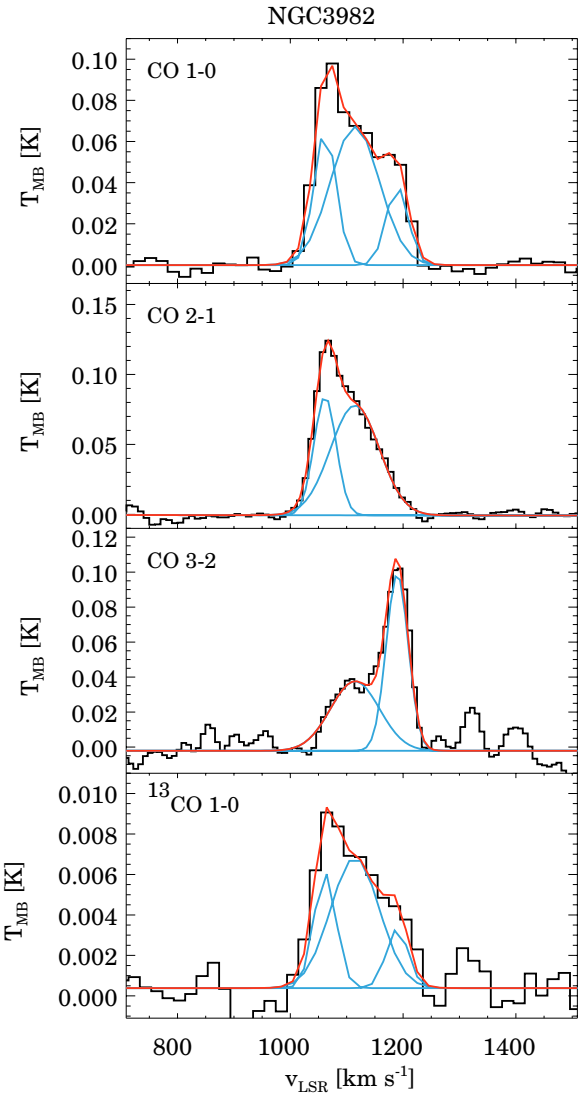

Figure 5. Same as Figure 3, but for NGC 3982. For this galaxy, the CO J = 3–2 transition was observed with the HHT 10 m.
(A color version of this figure is available in the online journal.)

assumed CO abundance with respect to H_2 in dense molecular clouds (Lacy et al. 1994; Hernandez & Tan 2011), Ω is the adopted SPIRE SLW beam size (1.66×10^{-8} sr), d is the distance to the galaxy, and m_{H_2} is the mass of an H_2 molecule. In Table 9, we present the calculated molecular gas masses.

4.2. Analysis of Individual Sources

4.2.1. UGC 05101

UGC 05101 is an IR bright galaxy ($L_{IR} = 10^{11.95}\,L_\odot$) located at 163 Mpc (Sanders et al. 2003). It has a peculiar morphology that suggests a recent interaction (Sanders et al. 1988). Its nuclear activity is classified as LINER from optical spectroscopy (Yuan et al. 2010). However, the detection of high-ionization emission lines in the mid-IR ([Ne V] and [O IV]; Armus et al. 2007), the intense Fe Kα emission line at 6.4 keV (Imanishi et al. 2003), and its high hard X-ray luminosity ($L_{2-10\,keV} = 7.5 \times 10^{42}$ erg s^{-1}; Imanishi et al. 2003) indicate the presence of a buried AGN with a luminosity comparable to that of a Seyfert galaxy.

In the SPIRE/FTS spectrum of this galaxy, we detect five unblended CO lines (see Table 3). An emission line is detected at the frequency of the CO J = 10–9 transition, but it is likely blended with the o-H_2O 3_{12}–2_{21} 1153 GHz line since water and CO emission lines have comparable fluxes in this galaxy. With the spectral resolution of SPIRE/FTS, it is not possible to deblend the two emission lines; therefore, we excluded it from the radiative transfer analysis.

In addition to the SPIRE/FTS data, we used ground-based observations of the low-J CO transitions to constrain the radiative models. Interferometric observations of the CO J = 1–0 line show that the CO emission is produced in a compact region (<1 kpc) plus a fainter extended (2.2 kpc) rotating disk (Genzel et al. 1998; Wilson et al. 2008).

The observed FWHM of the CO J = 3–2 line is 650 km s^{-1} (Iono et al. 2009). However, the SPIRE/FTS mid-J CO lines are spectroscopically unresolved, that is, the width of mid-J lines is <500 km s^{-1}. The line profile fitting of the CO J = 1–0, J = 2–1, and J = 3–2 transitions (Section 3.3.1) shows that the width of the middle component is 320 km s^{-1}, so we assumed that it is also the width of the mid-J CO lines. Consequently, we used in the CO SLED fit, presented in Figure 6, the CO J = 1–0, J = 2–1, and J = 3–2 fluxes of this middle component.

4.2.2. NGC 3227

NGC 3227 is a nearby (14.4 Mpc) Seyfert 1.5 galaxy (Ho et al. 1997). It is interacting with the dwarf elliptical galaxy NGC 3226. The hard X-ray luminosity of the AGN is 1.9×10^{41} erg s^{-1} (Gondoin et al. 2003). In addition, recent (∼40 Myr) intense star formation is observed in the nucleus. The luminosity produced by these young stars represents about half of the bolometric luminosity of the galaxy (Davies et al. 2006). The *Spitzer*/IRS mid-IR spectrum of this galaxy shows the [Ne V] and [O IV] high-ionization emission lines confirming the

Table 7
CO Line Fluxes from Ground-based Observations

Galaxy	CO $J = 1$–0 (10^{-16} erg cm^{-2} s^{-1})	Ref.[a]	CO $J = 2$–1 (10^{-16} erg cm^{-2} s^{-1})	Ref.[a]	CO $J = 3$–2 (10^{-16} erg cm^{-2} s^{-1})	Ref.[a]
NGC 1056	2.5 ± 0.5	1, I	10.4 ± 2.1	1, I	...	...
UGC 05101	1.8 ± 0.4	2, I	9.7 ± 2.0	2, I	22.5 ± 6.4	3, J
NGC 3227	6.1 ± 1.2	2, I	26.5 ± 5.3	2, I	125 ± 30	4, 2, H
NGC 3982	1.4 ± 0.3	2, I	4.3 ± 0.9	2, I	34.9 ± 13.0	4, 2, H
NGC 4051	5.6 ± 1.2	5, N	...	...	...	...
NGC 4151	...	...	3.0 ± 1.2	6, J	...	...
NGC 4388	1.7 ± 0.4	7, I	5.5 ± 1.7	7, I	...	...
IC 3639	2.2 ± 0.4	1, S	20.9 ± 4.2	1, S	...	...
NGC 7130	12.4 ± 2.5	1, S	44.8 ± 9.0	1, S	...	...
NGC 7172	13.3 ± 2.7	1, S	26.1 ± 5.2	1, S	...	...
NGC 7582	18.0 ± 3.7	8, S	139 ± 30	8, S	...	...

Notes. Fluxes and 1σ uncertainties of ground-based observations of the low-J CO lines. The fluxes were converted from their original units (K km s^{-1}) using the following relation: $F(\mathrm{erg\,cm^{-2}\,s^{-1}}) = I(\mathrm{K\,km\,s^{-1}})\ 9.197 \times 10^{-13} \nu(\mathrm{GHz})/(\pi \eta_{\mathrm{MB}}(R(\mathrm{cm}))^2)$, where ν is the transition frequency, η_{MB} is the main beam efficiency, and R is the radius of the telescope.
[a] Reference for the CO line flux and telescope used. (I) IRAM 30 m; (J) JCMT 15 m; (H) HHT 10 m; (N) NRO 45 m; (S) SEST 15 m.
References. (1) Albrecht et al. 2007; (2) This work (Section 3.3); (3) Wilson et al. 2008; (4) Mao et al. 2010; (5) Vila-Vilaró et al. 1998; (6) Rigopoulou et al. 1997; (7) Pappalardo et al. 2012; (8) Aalto et al. 1995.

Table 8
RADEX Models

Galaxy	Δv[a] (km s^{-1})	$\log T_{\mathrm{kin}}$[b] (K)	$\log n_{\mathrm{H_2}}$[c] (cm^{-3})	$\log\langle N_{\mathrm{CO}}\rangle$[d] (cm^{-2})	F_{CO}[e] (10^{-15} erg cm^{-2} s^{-1})
UGC 05101	320	2.9 ± 0.3	3.7 ± 0.4	15.2 ± 0.1	102 ± 11
NGC 3227	200	2.8 ± 0.1	3.3 ± 0.1	15.8 ± 0.1	190 ± 10
NGC 3982	100	2.0 ± 0.1	4.5 ± 0.4	15.2 ± 0.2	39 ± 4
NGC 4388	125	2.5 ± 0.2	3.9 ± 0.2	15.4 ± 0.1	104 ± 12
NGC 7130	90	2.8 ± 0.1	3.2 ± 0.1	16.1 ± 0.1	240 ± 10
NGC 7582	200	2.6 ± 0.2	3.6 ± 0.7	16.4 ± 0.2	540 ± 30

Notes. Best-fit parameters of the RADEX models.
[a] Line width assumed for the model.
[b] Kinetic temperature.
[c] Molecular hydrogen density.
[d] Beam-averaged CO column density. The beam FWHM is 30″.
[e] Integrated flux of the CO lines from $J_{\mathrm{up}} = 4$ to $J_{\mathrm{up}} = 12$ of the best-fit model.

Table 9
Molecular Gas Properties

Galaxy	$\log M_{\mathrm{warm}}$[a] ($M_\odot$)	$\log L_{\mathrm{CO}}$[b] ($L_\odot$)	$\log L_{\mathrm{H_2S(1)}}$[c] ($L_\odot$)	$L_{\mathrm{CO}}/M_{\mathrm{warm}}$[d] ($L_\odot/M_\odot$)	$\log M_{\mathrm{cold}}$[e] ($M_\odot$)	$\log M_{\mathrm{C}}$[f] ($M_\odot$)	x_{C}[g]
NGC 1056	...	...	6.1	...	8.3	4.6	5.6×10^{-5}
UGC 05101	7.7	7.9	8.0	1.4	9.5	6.4	1.5×10^{-4}
NGC 3227	6.2	6.1	6.3	0.6	8.0	4.7	4.1×10^{-4}
NGC 3982	5.9	5.7	5.6	0.6	7.6	4.4	1.3×10^{-4}
NGC 4051	...	...	5.8	...	8.0	4.0	2.5×10^{-5}
NGC 4151	...	...	5.4	...	...	3.8	...
NGC 4388	6.0	6.0	6.3	1.0	7.6	4.7	8.4×10^{-4}
IC 3639	...	...	6.4	...	8.5	4.8	4.8×10^{-5}
NGC 7130	7.8	7.5	7.1	0.4	9.6	6.0	1.7×10^{-4}
NGC 7172	...	...	6.8	...	9.0	5.8	3.6×10^{-4}
NGC 7582	7.0	6.9	6.7	0.6	8.7	5.1	1.8×10^{-4}

Notes. For the warm and cold molecular masses (M_{warm} and M_{cold}) listed in this table, we assumed $M_{\mathrm{mol}} = 1.4\, M_{\mathrm{H_2}}$ to account for He mass.
[a] Mass of the warm molecular gas traced by the mid-J CO lines (see Section 4.4).
[b] Integrated luminosity of the CO lines from $J_{\mathrm{up}} = 4$ to $J_{\mathrm{up}} = 12$ of the best-fit RADEX model (see also Table 8).
[c] Extinction corrected luminosity of the H_2 0–0 S(1) line at 17.03 μm.
[d] Warm molecular gas cooling rate per unit gas mass due to the CO transitions from $J_{\mathrm{up}} = 4$ to $J_{\mathrm{up}} = 12$.
[e] Mass of the cold molecular gas derived from the CO $J = 1$–0 line flux (see Section 4.3).
[f] Neutral carbon abundance with respect to H_2.
[g] Neutral carbon mass in the cold molecular clouds (Section 5).

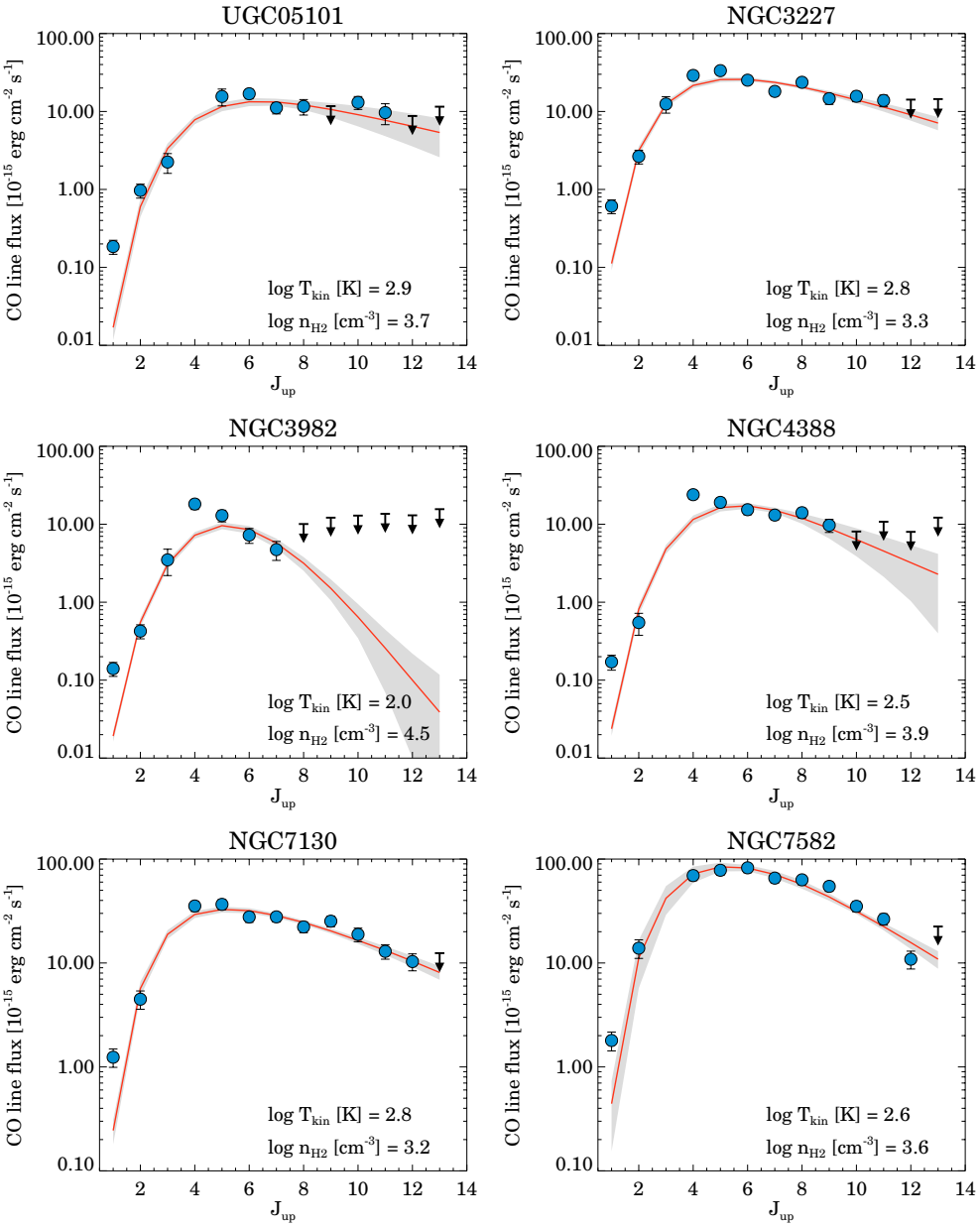

Figure 6. CO SLED (blue circles) and best-fit model (red line) for our galaxies. The shaded region is the 1σ uncertainty in the best-fit model calculated from the Monte Carlo simulations (see Section 4.1).

(A color version of this figure is available in the online journal.)

presence of an AGN (Deo et al. 2007; Dasyra et al. 2008; Weaver et al. 2010).

Interferometric observations of this galaxy (Schinnerer et al. 2000) show that part of the CO $J = 1$–0 and $J = 2$–1 emission is concentrated in a compact region of $\sim 8''$ of diameter ($\sim$500 pc).

In the FTS spectrum of NGC 3227, we detected the CO lines from $J_{up} = 4$ to $J_{up} = 11$. These CO emission lines are not resolved at the SPIRE/FTS spectral resolution; thus, we assumed the line width of the middle component of the CO $J = 1$–0 and $J = 2$–1 transitions, 200 km s^{-1} (see Section 3.3.1).

4.2.3. NGC 3982

NGC 3982 is a Seyfert 1.9 (Ho et al. 1997) located at 20.6 Mpc. The hard X-ray luminosity of this galaxy is $<2.5 \times 10^{39}$ erg s^{-1} and the Fe Kα feature at 6.4 keV is not detected (Guainazzi et al. 2005). This suggests that NGC 3982 hosts a relatively low luminosity AGN. Moreover, the luminosities of the high-ionization mid-IR [O IV] and [Ne V] emission lines are about 2×10^{39} erg s^{-1} (Tommasin et al. 2010), low compared to those of other Seyfert galaxies (see Figure 2 of Pereira-Santaella et al. 2010) and confirming that the AGN in NGC 3982 is not very luminous.

Four CO lines, from $J_{up} = 4$ to $J_{up} = 7$, are detected in the FTS spectrum of this galaxy, all of them in the SLW range. In the modeling, we included ground-based observations of the CO $J = 1$–0, $J = 2$–1, and $J = 3$–2 lines (see Section 3.3). The ground-based data show three kinematical components (see Figure 5 and Section 3.3.1). The width of the middle component is 100 km s^{-1}. The other two components are probably produced by a rotating disk. The difference in the relative intensities of the redshifted and blueshifted disk components from the $J = 2$–1 to the $J = 3$–2 transition are presumably due to pointing

uncertainty and the smaller beam size of the CO $J = 2$–1 observation. Mapping observations of these transitions would be needed to confirm this interpretation.

The best-fit model for NGC 3982 has a higher density and lower temperature than the rest of the galaxies (see Table 8 and Figure 6). No CO lines with $J_{up} > 7$ are detected, so our fit could be biased toward low kinetic temperatures. However, the CO $J = 4$–3/CO $J = 7$–6 ratio in NGC 3982 is more than a factor of two higher than in the other galaxies in the sample. This implies a lower kinetic temperature for a fixed density and, therefore, the estimated lower temperature is likely real and not a consequence of the limited sensitivity of the SPIRE/FTS spectrum.

4.2.4. NGC 4388

NGC 4388 is a nearby edge-on spiral galaxy located at 18.2 Mpc. A weak broad Hα component has been reported by Shields & Filippenko (1996) and it is classified as Seyfert 1.9 by Ho et al. (1997). However, Ruiz et al. (1994) did not find evidence for broad components in the near-IR Paβ line. A hidden broad line region (HBLR) is detected in optical polarized light (Young et al. 1996). Both the mid-IR [Ne v] and [O iv] high-ionization emission lines are detected in the *Spitzer*/IRS spectrum of this galaxy (Tommasin et al. 2010). The absorption corrected hard X-ray luminosity of the AGN is 3.0×10^{41} erg s^{-1} (Cappi et al. 2006). A radio jet is observed in this galaxy (Falcke et al. 1998).

We detect six CO lines from $J_{up} = 4$ to 9 in the SLW SPIRE/FTS spectrum. We obtained ground-based measurements of the CO $J = 1$–0 and $J = 2$–1 fluxes from the literature (Pappalardo et al. 2012, see Section 3.3). For the line width, we assumed 125 km s^{-1} (Vila-Vilaró et al. 1998). The best-fit model is shown in Figure 6.

4.2.5. NGC 7130

NGC 7130 is an LIRG ($L_{IR} = 10^{11.35}\ L_{\odot}$) located at 66 Mpc (Sanders et al. 2003). Its nuclear activity is classified as Seyfert 2 (Yuan et al. 2010). It is a face-on spiral galaxy with a disturbed morphology. Faint tidal tails are observed, although there are no nearby companions. It hosts a Compton-thick AGN with an estimated intrinsic hard X-ray luminosity of 8.3×10^{40} erg s^{-1} (Levenson et al. 2005). *Spitzer*/IRS observations show the detection of the [Ne v] and [O iv] high-ionization emission lines (Tommasin et al. 2010). In addition to the powerful AGN, a strong burst of star formation is taking place in the nuclear region of this galaxy (González Delgado et al. 2001; Díaz-Santos et al. 2010).

In the SPIRE/FTS spectrum of NGC 7130, we measured nine CO lines from $J_{up} = 4$ to 12. We fitted the lines observed with SPIRE/FTS together with the CO $J = 1$–0 and CO $J = 2$–1 fluxes obtained from the literature (Albrecht et al. 2007). The CO line width is ∼90 km s^{-1} (Albrecht et al. 2007).

The CO $J = 10$–9 line was excluded from the fit because it could be blended with the H_2O 3_{12}–2_{21} line. However, the best-fit model explains the observed flux of the CO $J = 10$–9 line, and therefore the contribution of the water line is likely small (see Figure 6).

4.2.6. NGC 7582

NGC 7582 is a Seyfert galaxy at a distance of 20.6 Mpc. It is a member of the interacting Grus Quartet (de Vaucouleurs 1975). The nuclear activity is classified as Type 2 because no broad lines are detected in the optical (Heisler et al. 1997). However, Reunanen et al. (2003) reported a broad component in the near-IR Brγ line. The hard X-ray luminosity of the AGN is 2.0×10^{41} erg s^{-1} (Piconcelli et al. 2007). The nuclear region of NGC 7582 harbors young star-forming regions that dominate the ionization of the nuclear gas (Riffel et al. 2009). In the mid-IR *Spitzer*/IRS spectrum of NGC 7582, the [Ne v] and [O iv] high-ionization emission lines are detected (Tommasin et al. 2010).

The CO lines from $J_{up} = 4$ to 12 are detected in the SPIRE/FTS data. We added to the CO SLED ground-based observations of the CO $J = 1$–0 and $J = 2$–1 lines (Aalto et al. 1995). For the line width, we used ∼200 km s^{-1} (Baan et al. 2008).

The nuclear far-IR emission of this galaxy is only partially resolved at the resolution of *Herschel*, so the effects of the different SPIRE/FTS beam sizes are minimized. Therefore, we fitted all the CO lines simultaneously (Figure 6).

4.3. Cold Molecular Gas

From Figure 6, we see that the best-fit models for the warm molecular gas components ($T_{kin} \sim 500$ K; see Section 4.4) underpredict the flux of the CO $J = 1$–0 line. The predicted fluxes are 10%–25% of the observed values. This CO $J = 1$–0 excess is explained if a cold gas component is also present in these galaxies.

The beam-averaged H_2 column density of the cold component can be estimated using the CO-to-H_2 conversion factor $N_{H_2}(\mathrm{cm}^{-2}) = 0.5 \times 10^{20} I_{CO\,J=1-0}$ (K km s^{-1}) revised for active galaxies (Downes & Solomon 1998). Substituting in Equation (1), we obtain: $M_{mol}(M_{\odot}) \sim 7 \times 10^{20} F_{CO\,J=1-0}(\mathrm{erg\ cm^{-2}\ s^{-1}}) \times (d(\mathrm{Mpc}))^2$. We subtracted the contribution of the warm component to the CO $J = 1$–0 line for the six galaxies modeled. For the rest of the galaxies, this contribution to the CO $J = 1$–0 emission introduces an extra ∼25% uncertainty in the cold molecular mass. The calculated masses are listed in Table 9; they range from $10^{7.6}$ to $10^{9.5}\ M_{\odot}$.

4.4. Warm Molecular Gas

From the RADEX modeling of the low- and mid-J CO lines, we find that the CO SLEDs of five out of the six galaxies analyzed (all except NGC 3982) can be fitted with a warm gas component with comparable physical properties, $n_{H_2} \sim 10^{3.2}$–$10^{3.9}$ cm^{-3} and $T_{kin} \sim$ 300–800 K (see Table 8).

Similar analysis of the mid-J CO SLED have been presented for Arp 220, M 82, and NGC 1068 (Rangwala et al. 2011; Kamenetzky et al. 2012; Spinoglio et al. 2012). In these galaxies, two or more CO components are fitted to the SLED; therefore, we compare our results with their warm gas component. The gas density and temperature in our galaxies are close to those of the starburst M 82 ($n_{H_2} = 10^{3.4}$ cm^{-3} and $T_{kin} = 500$ K). In the ultraluminous IR galaxy (ULIRG) Arp 220, the warm molecular gas has a higher temperature, $T_{kin} = 1300$ K, and a slightly lower density, $n_{H_2} = 10^{3.2}$ cm^{-3}, although within the uncertainties, both parameters are comparable to the values of our galaxies. In contrast, the warm molecular gas traced by the mid-J CO lines in NGC 1068 has a lower temperature, 90 K, and higher density, $10^{4.6}$ cm^{-3}.

We use Equation (1) to calculate the molecular mass. The resulting masses are listed in Table 9. They range from 10^6 to $10^8\ M_{\odot}$. These masses are lower than the warm molecular component observed in Arp 220, $10^{8.7}\ M_{\odot}$, but resemble those

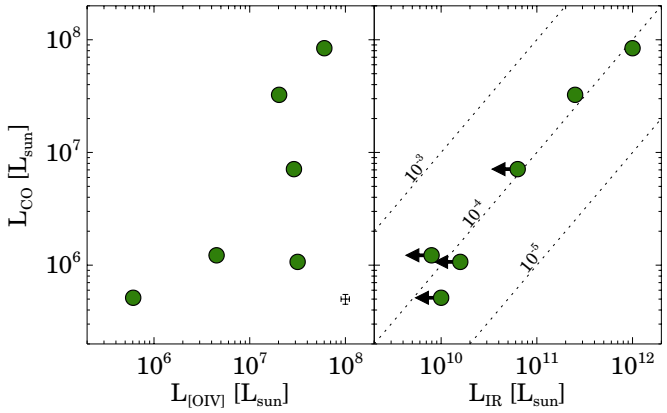

Figure 7. Mid-*J* CO luminosity vs. [O IV]25.9 μm luminosity (left panel) and vs. IR luminosity (right panel). The [O IV]25.9 μm luminosity is a proxy of the AGN luminosity in Seyfert galaxies, whereas the IR luminosity traces the star formation rate. The dashed lines in the right panel show the L_{CO}/L_{IR} ratio. The [O IV]25.9 μm fluxes are from the Pereira-Santaella et al. (2010) compilation.

(A color version of this figure is available in the online journal.)

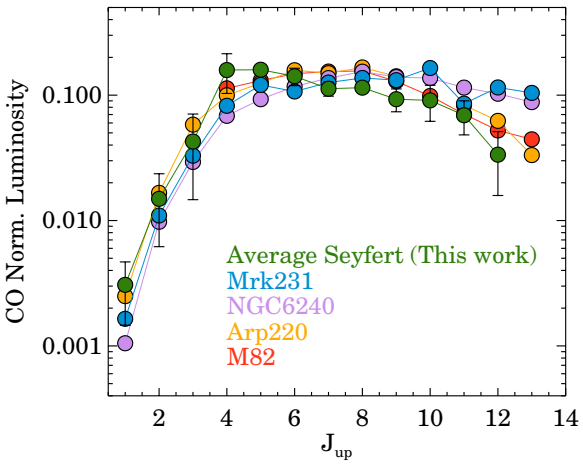

Figure 8. CO SLEDs normalized to the integrated CO luminosity (from $J_{up} = 1$ to $J_{up} = 12$). We compare the average CO SLED of our Seyfert galaxies with those of Mrk 231 (van der Werf et al. 2010), NGC 6240 (Meijerink et al. 2013), Arp 220 (Rangwala et al. 2011), and M 82 (Kamenetzky et al. 2012).

(A color version of this figure is available in the online journal.)

observed in M 82 and NGC 1068, $10^{6.2}$ $M_\odot$ and $10^{7.4}$ $M_\odot$, respectively. For these six galaxies, the mass of the cold molecular gas (Section 4.3) is between 40 and 120 times higher than that of the warm component, whereas in Arp 220 and M 82 the cold-to-warm molecular gas mass ratio is smaller, ∼10.

Warm molecular gas is also traced by the mid-IR rotational H_2 lines. The gas temperatures derived from the lowest H_2 rotational transitions are 100–1000 K (Rigopoulou et al. 1999; Roussel et al. 2007) and are similar to the temperature range obtained from our radiative transfer analysis. Therefore, the mid-*J* CO lines and the rotational H_2 lines might trace the same warm molecular clouds.

The rotational H_2 0–0 S(1) line at 17.03 μm is expected to account for 15%–80% of the total H_2 emission arising from the warm molecular gas (based on the Shaw et al. 2005 models) depending on the gas temperature and density. Indeed, the H_2 S(1) is usually the brightest H_2 line in the mid-IR *Spitzer*/IRS spectra of galaxies (e.g., Roussel et al. 2007). For most of the galaxies in our sample, H_2 S(1) fluxes were presented by Tommasin et al. (2008, 2010).[14] To correct for dust extinction first, we estimated A_K using the relation $A_K/\tau_{9.7} = 1.48$ (McClure 2009), where $\tau_{9.7}$ is the optical depth of the 9.7 μm silicate absorption feature. The $\tau_{9.7}$ values of our galaxies were published by Wu et al. (2009). Then, assuming $A_{17\,\mu m} \sim 0.4 \times A_K$ (McClure 2009), we corrected the H_2 S(1) fluxes. In Table 9, we compare the extinction corrected luminosity of this line with the integrated luminosity of the mid-*J* CO lines ($J_{up} = 4$ to $J_{up} = 12$, those in the spectral range observed by SPIRE/FTS). The total H_2 luminosity is 0.1–0.8 dex higher than the H_2 S(1) luminosity depending on the exact gas conditions. So, in general, the H_2 cooling is higher but comparable to the mid-*J* CO cooling in these galaxies.

Table 9 also shows the ratio between the integrated luminosity of the mid-*J* CO lines and the molecular gas mass (L_{CO}/M_{mol}). This ratio is between 0.4 and 1.3 $L_\odot/M_\odot$ in our galaxies, similar to the CO cooling ratio measured in the warm CO component of Arp 220 (0.4 $L_\odot/M_\odot$, Rangwala et al. 2011). For the gas conditions derived from the modeling, the expected H_2 cooling ratio is ∼0.5–10 $L_\odot/M_\odot$ (Le Bourlot et al. 1999). These values agree with the observed rotational H_2 cooling; thus, this supports the idea that the mid-IR rotational H_2 lines and the mid-*J* CO lines originate in the same warm molecular gas. This agreement also indicates that the CO abundance ($x_{CO} = 3 \times 10^{-4}$) used to calculate the M_{mol} is reasonable for the warm molecular gas in these active galaxies.

4.5. Warm CO Heating Source

Our radiative transfer modeling shows that warm molecular gas contributes significantly to the CO luminosity in these Seyfert galaxies. To determine the heating source of the warm gas in Figure 7, we compare the mid-*J* CO luminosity with the [O IV]25.9 μm luminosity, a proxy of the AGN luminosity (Meléndez et al. 2008), and the IR luminosity,[15] which is correlated with the star formation rate (Kennicutt 1998). There is no clear correlation between the AGN luminosity and the CO luminosity (left panel). For $L_{[O\,IV]} \sim 5 \times 10^7\,L_\odot$, the CO luminosity differs two orders of magnitude from galaxy to galaxy. On the other hand, the L_{CO} seems consistent with an L_{CO}/L_{IR} ratio of about 10^{-4}. That is, the mid-*J* CO emission is more likely related to the star formation activity than to the AGN luminosity in our sample of Seyfert galaxies.

PDRs are expected in star-forming regions where UV photons from young stars heat the ISM; therefore, we compared the observed CO SLEDs with the PDR models of Wolfire et al. (2010). However, we find that no single PDR model reproduces the observed CO SLED. In general, the best-fit PDR models underpredict the fluxes of the CO lines with $J_{up} > 8$ lines. Conversely, XDR models (Meijerink et al. 2006) better reproduce the higher *J* CO lines and slightly underpredict those with $J_{up} < 6$. Consequently, we cannot rule out an XDR contribution to the higher *J* CO emission in our galaxies.

In Figure 8, we compare the average CO SLED of our Seyfert galaxies with those published for other galaxies. The luminosity

[14] For UGC 05101 the H_2 S(1) flux was published by Farrah et al. (2007). For NGC 3227 and NGC 4151, S. Tommasin provided us with the H_2 S(1) fluxes measured from the high spectral resolution *Spitzer*/IRS spectra following the method described in Tommasin et al. (2010). The H_2 S(1) fluxes are $(26.8 \pm 0.2) \times 10^{-14}$ and $(5.44 \pm 0.82) \times 10^{-14}$ erg cm^{-2} s^{-1} for NGC 3227 and NGC 4151, respectively.

[15] The L_{IR} values in Table 1 are calculated from *IRAS* fluxes. *IRAS* beams are much larger than the SPIRE/FTS beam, thus for the galaxies with the larger apparent sizes (see Figure 1) we consider this L_{IR} as an upper limit.

normalized CO SLEDs are visibly very similar up to $J_{up} = 11$. Only for $J_{up} > 11$, the CO emission in Mrk 231 and NGC 6240 is approximately a factor of three brighter than in the rest of the galaxies. For the Seyfert 1 Mrk 231, an XDR is proposed to explain the CO $J_{up} > 10$ emission and two PDR to model the lower-J CO emission (van der Werf et al. 2010), whereas for the merger galaxy NGC 6240, shock excitation can explain its complete CO SLED (Meijerink et al. 2013). For Arp 220, PDR, XDR, and cosmic rays heating mechanisms are ruled out and mechanical energy from supernovae is suggested as the heating source (Rangwala et al. 2011). For M 82, a combination of PDR and shocks is required to explain the observed CO emission (Kamenetzky et al. 2012). That is, the mid-J CO emission of galaxies, at least up to $J_{up} \sim 11$, seems to be produced by warm molecular gas with similar average physical conditions, although it can be heated by different combinations of mechanisms (PDR, XDR, cosmic rays, and shocks).

5. [C I] 492 AND 809 GHz EMISSION

PDR models predict that the two [C I] lines at 492 and 809 GHz are produced in the transition region from C^+ to CO that occurs in a relatively thin layer within the molecular clouds (Kaufman et al. 1999; Bolatto et al. 1999). However, some observational evidence suggests that neutral carbon and CO can coexist in the same volume (see Papadopoulos et al. 2004 and references therein). The latter can be achieved due to non-chemical equilibrium between C^0 and CO (Papadopoulos et al. 2004; Glover et al. 2010) or turbulent diffusion of the neutral carbon layer into the interiors of the molecular clouds (Xie et al. 1995). Moreover, cosmic rays and X-ray radiation also increase the C^0/CO abundance ratio throughout the clouds (Papadopoulos et al. 2004; Meijerink et al. 2006).

For five of the galaxies in our sample, we detect both [C I] fine structure emission lines at 492 and 809 GHz. For the rest, we detect only the [C I] line at 809 GHz (see Table 3). This is in part because the 492 GHz emission line lies in a noisy part of the SLW spectra, but also because it seems to be weaker than the 809 GHz line (at least in the galaxies with both [C I] lines detected).

To investigate the origin of the [C I] emission in these galaxies, we used RADEX to calculate the fluxes of the [C I]492 GHz and 809 GHz lines for a wide range of physical conditions ($n_{H_2} = 10$–10^8 cm^{-3}, $T = 10$–1000 K, and $N_C/\Delta v = 10^{12}$–10^{18} cm^{-2}/(km s^{-1})). We considered C^0 collisions with H_2 using the collisional rate coefficients of Schroder et al. (1991).

In Figure 9, we plot the expected [C I]809 GHz/[C I]492 GHz ratio as a function of the molecular hydrogen density and kinetic temperature for optically thin emission. The solid lines represent the observed ratios for the five galaxies with both lines detected. They span a narrow range in our sample, from 1.2 to 2.2. These [C I]809 GHz/[C I]492 GHz ratios indicate a kinetic temperature about 19–27 K if the gas density is higher than the critical densities of the neutral carbon lines ($n_{H_2} > 10^4$ cm^{-3}). For lower gas densities, the temperature is not well constrained since this ratio would be compatible with that of higher temperature ($T_{kin} > 50$ K) diffuse clouds (lower right corner in Figure 9).

To test if the [C I] emission arises from the warm molecular gas component traced by the mid-J CO lines, we plotted the derived physical conditions of the warm gas (see Section 4) in Figure 9. Under these conditions, the expected [C I]809 GHz/[C I]492 GHz ratio is 6–8, more than three times the observed ratio, so the bulk of the neutral carbon emission is not likely to be produced in the warm molecular gas component.

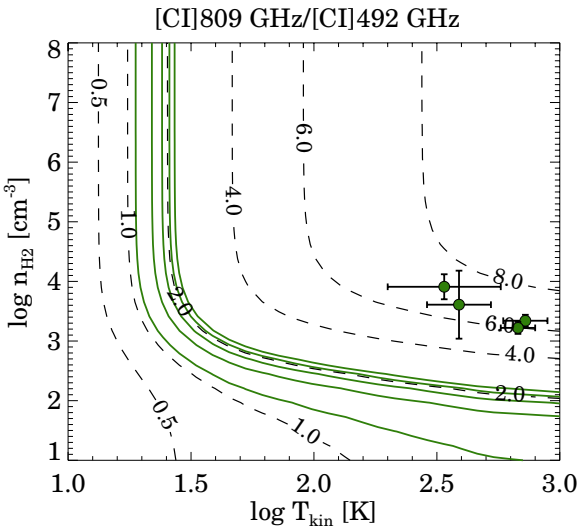

Figure 9. Dashed black lines are the [C I]809 GHz/[C I]492 GHz ratio (fluxes in erg cm^{-2} s^{-1} sr^{-1}) as a function of the H_2 density (n_{H_2}) and kinetic temperature (T_{kin}) in the optically thin limit. The solid green lines are the ratios measured in our sample of galaxies. The green circles represent the molecular gas conditions derived from the mid-J CO lines (see Section 4). UGC 05101 is not included in this figure because only the [C I]809 GHz line is detected in this galaxy.

(A color version of this figure is available in the online journal.)

Instead, the [C I] emission can originate in the cold gas component traced by the CO $J = 1$–0 line (see Section 4.3). Actually, there is a good correlation between the C^0 and CO $J = 1$–0 intensity in our Galaxy (Ikeda et al. 2002; Ojha et al. 2001) and nearby galaxies (Wilson 1997). However, the ratio between the CO and [C I] emissions depends on the specific physical conditions (UV flux, cosmic-ray rate, turbulence, etc.) in the molecular clouds (Israel & Baas 2002; Papadopoulos et al. 2004).

We used the RADEX grid of models to calculate the C^0 mass and column density in these cold molecular clouds. We assumed that the neutral carbon emission is optically thin and thermalized ($n_{H_2} > 10^4$ cm^{-2}). From the [C I]809 GHz/[C I]492 GHz ratio, we estimated the gas temperature (see Figure 9). When the [C I]492 GHz line is not detected, we assumed $T_{kin} = 23$ K (the median T_{kin} for the galaxies with both [C I] lines detected). Then, we compared the observed [C I]809 GHz luminosity with the predicted value to estimate the C^0 column densities and masses. The derived C^0 masses range from $10^{3.8}$ to $10^{6.3}$ $M_\odot$ (Table 9). In Section 4.3, we calculated the mass of the cold molecular component; therefore, using the information that the relative weight of C^0 and H_2 is 6, we determine that the C^0 abundance relative to H_2 in these galaxies is $\sim 3\times10^{-5}$–8×10^{-4}. Consequently, the C^0/CO abundance ratio ranges from 0.1 to 2 (assuming $x_{CO} = 3 \times 10^{-4}$). These C^0/CO abundance ratios are comparable to those measured in quiescent nearby galaxies (Israel & Baas 2002) and starbursts (Rangwala et al. 2011; Kamenetzky et al. 2012). However, it should be noted that these C^0 abundances rely on the CO-to-H_2 conversion factor that can vary by up to a factor of ~4 from galaxy to galaxy (e.g., Downes & Solomon 1998).

The C^0 abundance is expected to be enhanced in XDRs with respect to that in PDRs (Meijerink et al. 2006). For a constant gas density, Meijerink et al. (2006) models predict higher [C I]492 GHz/CO $J = 1$–0 intensity ratios in XDRs than in PDRs. In these PDR models, the [C I]492 GHz/CO $J = 1$–0 ratio ranges between 20 and 170, decreasing with increasing gas

densities, whereas in XDR models this ratio is between 50 and 10^5. In most of our galaxies, the [C I]492 GHz/CO $J = 1$–0 ratios are between 15 and 40, so they are compatible with PDR excitation. Only in NGC 4388, the [C I]492 GHz/CO $J = 1$–0 ratio is higher, 85 ± 20. This ratio can be explained by PDR models, but also by a high-density ($n = 10^5$ cm^{-3}) XDR model. Therefore, in most of our sample, the C^0 emission is consistent with that expected from PDRs, although for one galaxy XDR excitation is possible.

6. HYDROGEN FLUORIDE

The HF $J = 1$–0 transition at 1232 GHz has been recently detected in the SPIRE/FTS spectra of several local galaxies: the ULIRGs Mrk 231 (van der Werf et al. 2010) and Arp 220 (Rangwala et al. 2011); the starburst M 82 (Kamenetzky et al. 2012); and the Seyfert 2 NGC 1068 (Spinoglio et al. 2012). This transition has also been observed in the Cloverleaf quasar at $z = 2.46$ (Monje et al. 2011). In our sample, we detect this line in UGC 05101 in absorption, and in NGC 7130 in emission (see Table 4).

Hydrogen fluoride molecules are rapidly formed by the reaction of F with molecular hydrogen when the latter becomes abundant, so it is a good proxy for molecular gas. Most of the fluorine in molecular clouds is present as hydrogen fluoride, and in diffuse clouds HF can be several times more abundant than CO (Neufeld et al. 2005).

Owing to the high critical density of the HF $J = 1$–0 transition ($n_{H_2} \sim 10^{10}$ cm^{-3} at 50 K; Neufeld et al. 2005), it is expected to be observed in absorption. However, IR radiative pumping[16] can populate levels with $J \geqslant 1$, and thus it would be possible to observe the $J = 1$–0 transition in emission (Neufeld et al. 2005). Alternatively, HF can be formed in excited states that lead to the emission of the $J = 1$–0 line. This mechanism, chemical pumping, is possible in strong UV radiation fields, where HF photodissociation and formation rates are high (van der Tak 2012). In addition, since HF has a large dipole moment, collisions with electrons can excite its rotational levels (van der Tak et al. 2012).

6.1. UGC 05101

We detect the HF $J = 1$–0 transition in absorption in UGC 05101. Assuming that this transition is optically thin, we calculated the HF column density using the following equation (see Draine 2011):

$$N_l(\mathrm{cm}^{-2}) = 9.33 \times 10^5 \frac{W_\lambda(\mathrm{cm})\,(\nu_{ul}\,(\mathrm{GHz}))^4}{A_{ul}(\mathrm{s}^{-1})} \frac{g_l}{g_u}, \quad (2)$$

where N_l is the column density of the lower energy level, A_{ul} is the Einstein coefficient, W_λ is the equivalent width of the line, and g_u and g_l are the degeneracy of the upper and lower levels, respectively. For the HF $J = 1$–0 transition, $A_{10} = 2.42 \times 10^{-2}$ s^{-1}, $g_1 = 3$, and $g_0 = 1$, and $\nu_{10} = 1232.476$ GHz (from the Leiden Atomic and Molecular Database [LAMDA]; Schöier et al. 2005). In UGC 05101, the continuum at the frequency of the HF $J = 1$–0 line is 5.4 ± 0.2 Jy, so $W_\lambda = (3.8 \pm 0.9) \times 10^{-6}$ cm. Substituting in Equation (2), we obtain $N_0 = (1.1 \pm 0.3) \times 10^{14}$ cm^{-2}. This column density should be considered a lower limit because (1) the measured equivalent width is a lower limit, since we assumed that all the observed continuum at 1232 GHz illuminates the molecular clouds that produce the HF absorption and this might not be true; (2) we can only observe the HF in molecular clouds in front of the far-IR continuum source in our line of sight; and (3) we do not consider HF molecules in excited energy levels, although most of the HF molecules are expected to be in the ground energy level (see Neufeld et al. 2005).

[16] Ground-state HF can be excited by 2.5 μm near-IR photons to its first vibrational level, that then can decay to excited rotational levels of the ground vibrational state.

6.2. NGC 7130

In NGC 7130, the HF $J = 1$–0 transition is detected in emission. In this section, we discuss three possible excitation mechanisms to explain the HF $J = 1$–0 emission line in this galaxy.

First, we calculated the column density of the upper level assuming that the HF emission is optically thin. This value is independent of the excitation mechanism. Using RADEX, we verified that the optically thin approximation is valid for a wide range of physical conditions ($T_{\mathrm{kin}} = 5$–250 K, $n_{H_2} = 10$–10^{10} cm^{-3}, and $N_{\mathrm{HF}} = 10^8$–10^{13} cm^{-2} for $\Delta v = 90$ km s^{-1}). Therefore, we can use following relation to calculate the column density of the $J = 1$ level:

$$\langle N_u \rangle = \frac{4\pi}{\Omega} \frac{F_{ul}}{h\nu_{ul} A_{ul}}, \quad (3)$$

where $\langle N_u \rangle$ is the beam-averaged column density of the upper transition level, Ω is the beam solid angle, F_{ul} is the line flux in erg cm^{-2} s^{-1}, and h is the Planck constant. For the HF $J = 1$–0 line, the beam FWHM is 18″, thus $\langle N_1 \rangle = (9.1 \pm 1.2) \times 10^{10}$ cm^{-2}. This column density is a lower limit to the total HF column density since we have only considered the molecules in the $J = 1$ rotational level.

6.2.1. IR Pumping

Carroll & Goldsmith (1981) show that IR pumping can efficiently increase the population of ground state rotational levels when

$$\frac{f}{e^{h\nu/kT} - 1} > \frac{A_{J+1,J}}{A_{\nu,\nu-1}}, \quad (4)$$

where f is a factor to account for the geometric dilution and dust emissivity, ν is the frequency of the vibrational transition, T is the radiation field temperature, and $A_{J+1,J}$ and $A_{\nu,\nu-1}$ are the Einstein coefficients for the rotational and vibrational transitions, respectively. For the lowest vibrational transition, $A = 63.2$ s^{-1} and $h\nu/k = 5756$ K (LAMDA). Therefore, assuming that the near-IR radiation seen by the HF molecules completely fills the sky ($f = 1$), the required minimum radiation field temperature for efficient IR pumping is $T > 730$ K. This corresponds to an energy density $\nu u_\nu \sim 5 \times 10^{-4}$ erg cm^{-3} at 2.5 μm, that is, a radiation field $>10^6$ times that in a PDR near ($d = 0.2$ pc) an O star (Draine 2011). If $f < 1$, then the radiation temperature, and energy density, would be higher. Consequently, if the HF molecules are excited by IR pumping in NGC 7130, then they should be illuminated by a very intense IR radiation field that can be produced only by the AGN.

6.2.2. Chemical Pumping

To be efficient, chemical pumping requires that the number of HF molecules formed exceeds the number of spontaneous decays from the $J = 1$ to the $J = 0$ levels (see van der Tak

2012). This condition can be expressed as

$$R\frac{N_{\rm HF}}{n_{\rm HF}} \geqslant A_{10}N_1, \quad (5)$$

where R is the formation rate, $N_{\rm HF}$ is the total HF column density, $n_{\rm HF}$ is the HF density, and N_1 is the column density of the HF molecules in the $J = 1$ level. Assuming that HF formation and destruction are balanced:

$$R = kn_{\rm H_2}n_{\rm F} = n_{\rm HF}\zeta_d\chi, \quad (6)$$

where $k = 2.86 \times 10^{-12}$ cm^3 s^{-1} is the HF formation rate at 50 K, $\zeta_d = 1.17 \times 10^{-10}$ s^{-1} is the HF photodissociation rate for $\chi_{\rm UV}$, the standard interstellar UV radiation field of Draine (1978; Neufeld et al. 2005), χ is the UV radiation field in units of $\chi_{\rm UV}$, and $n_{\rm HF}$ and $n_{\rm F}$ are the densities of hydrogen fluoride and atomic fluorine, respectively. Since $n_{\rm HF} + n_{\rm F} = 2\mathcal{A}_{\rm F}n_{\rm H_2}$, where $\mathcal{A}_{\rm F} = 2.9 \times 10^{-8}$ is the solar F abundance with respect to H (Lodders 2003), Equation (5) can be rewritten as

$$\frac{\zeta_d\chi}{A_{10}}\frac{2\mathcal{A}_{\rm F}kn_{\rm H_2}}{\zeta_d\chi + kn_{\rm H_2}}N_{\rm H_2} \geqslant N_1. \quad (7)$$

For the conditions in a PDR ($\chi = 10^3$, $n_{\rm H_2} = 10^4$ cm^{-3}), the N_1 calculated before implies an $N_{\rm H_2} > 10^{24}$ cm^{-2}. That is several orders of magnitude higher than the H_2 column density derived from the CO $J = 1$–0 transition (see Section 4.3). Both higher gas densities and more intense radiation fields decrease the minimum H_2 column density. Only a combination of dense gas ($n_{\rm H_2} > 10^7$ cm^{-3}) and intense UV radiation fields ($\chi > 10^7$) is compatible with the derived H_2 column density in NGC 7130. This intense UV radiation field suggests that the HF molecules should be close to the AGN.

6.2.3. Collisional Excitation by Electrons

The rotational levels of molecules are usually excited by collisions with H_2. However, for molecules with a large dipole moment, like HF, the rotational levels can be excited by collisions with electrons as well. In general, in the interior of molecular clouds, where most of the molecules are found, the electron abundance is low ($n_{\rm e}/n_{\rm H_2} < 10^{-6}$; see Figure 1 of Meijerink et al. 2006) and the collisions with electrons can be neglected. However, in some situations, like diffuse clouds (Black & van Dishoeck 1991), and molecular clouds surfaces (Wolfire et al. 2010), or XDRs (Meijerink et al. 2006), the electron density is enhanced. The majority of the free electrons in molecular clouds come from ionized carbon, with a small contribution from hydrogen ionized by cosmic rays (Liszt 2012). Therefore, the electron abundance can be as high as $n_{\rm e}/n_{\rm H} \sim 1.6 \times 10^{-4}$, that is, the gas-phase carbon abundance (Sofia et al. 2004).

The HF $J = 1$–0 critical density for collisions with electrons at 50 K is $n_{\rm e} = 1.7 \times 10^4$ cm^{-3} (calculated using the LAMDA electron-HF collision strengths). Taking the highest $n_{\rm e}$ abundance calculated above, this critical density is reached when $n_{\rm H_2} = 10^8$ cm^{-3}. This is two orders of magnitude lower than the critical density for collisions with H_2, but it is still high. Hence, the HF $J = 1$–0 emission line is thermalized only in high-density molecular clouds.

Similar to van der Tak et al. (2012), we used RADEX to model the HF emission taking into account collisions with both molecular hydrogen and electrons. We computed a grid of models for $n_{\rm H_2} = 10^2$–10^{11} cm^{-3}, $T_{\rm kin} = 10$–250 K, and $n_{\rm e}/n_{\rm H_2} = 10^{-4}$. We used the electron-HF collisional rate coefficients from LAMDA calculated by van der Tak et al. (2012) using the Coulomb–Born approximation. The HF $J = 1$–0 line is optically thin for a wide range of physical conditions, so the line flux will be proportional to $N_{\rm HF}$ in the escape probability approximation. That is,

$$F\ ({\rm erg\ cm^{-2}\ s^{-1}\ sr^{-1}}) = \mathcal{K}N_{\rm HF}\ ({\rm cm^{-2}}), \quad (8)$$

where $\mathcal{K}$ depends on the density of the collisional partners, electrons and molecular hydrogen, and on the kinetic temperature.

For gas densities between $n_{\rm H_2} = 10^3$–10^4 cm^{-3} and $T_{\rm kin} > 50$ K, $\mathcal{K}$ ranges between 10^{-22} and 10^{-21}. The HF $J = 1$–0 flux in NGC 7130 is 1.4×10^{-6} erg cm^{-2} s^{-1} sr^{-1} (assuming the SLW beam size, 18″, as the source size). Accordingly, this corresponds to a beam-averaged HF column density $>10^{15}$ cm^{-2}. Given the F abundance, $\mathcal{A}_{\rm F} = 2.9 \times 10^{-8}$, the resulting $\langle N_{\rm H_2}\rangle$ would be unrealistically high. For lower $T_{\rm kin}$, $\mathcal{K}$ values are lower, $\sim$$10^{-24}$–$10^{-23}$, and the column density would be even higher.

In the high-density limit ($n_{\rm H_2} > 10^8$ cm^{-3}), where HF would be thermally excited, $\mathcal{K}$ is $\sim$$10^{-18}$. Therefore, for the observed HF flux in NGC 7130, we obtain $\langle N_{\rm HF}\rangle \sim 10^{12}$ cm^{-2} and $\langle N_{\rm H_2}\rangle \sim 10^{20}$ cm^{-2}. It would imply $\sim 4 \times 10^7$ $M_\odot$ of very high density molecular gas, where C is single ionized. This region would correspond to the dark molecular gas (that does not emit in CO), which represents about 30% of the total gas in PDRs (Wolfire et al. 2010). However, typical PDR densities are $n_{\rm H_2} \sim 10^4$ cm^{-2}, much lower than the high-density gas where HF would be excited by electron collisions. These densities are reached in dense molecular cores, but there the UV field is shielded and ionized carbon is not expected. Therefore, the gas where the HF $J = 1$–0 line originates does not seem to be related to the star formation activity in this galaxy. On the contrary, X-rays from the AGN can keep a high ionization fraction over large column densities (González-Alfonso et al. 2013). The importance of X-ray ionization in NGC 7130 is also supported by the detection of several OH^+ transitions in its FTS spectrum (see Section 7.2).

6.2.4. HF Excitation in NGC 7130

We discussed three possible excitation mechanisms to explain the HF $J = 1$–0 emission in NGC 7130. These mechanisms require high-density molecular gas, in addition to strong near-IR or UV emission for the IR and chemical pumping, respectively. Although our analysis does not favor any of these mechanisms over the rest, the physical conditions of the gas are not similar to those expected in star-forming regions (PDRs). Consequently, the HF $J = 1$–0 emission in NGC 7130 appears to be related to the AGN activity.

7. OTHER MOLECULES

7.1. Water

We detected ortho- and para-water (o- and p-H_2O) transitions in four of our galaxies: two lines in UGC 05101, one in NGC 3227, four in NGC 7130, and one in NGC 7582 (see Table 3). All the transition are detected in emission. These water lines are weaker than the CO lines present in the SPIRE/FTS spectra of these Seyfert galaxies. This is also the case in the starburst galaxy M 82 and the Seyfert 2 NGC 1068 (see Kamenetzky et al. 2012; Spinoglio et al. 2012). On the contrary, in the ULIRG Arp 220, water lines are more intense than the mid-J CO lines (Rangwala et al. 2011).

To model the excitation of water using radiation transfer models, we would need to detect more water transitions in each galaxy (see, e.g., Spinoglio et al. 2012; González-Alfonso et al. 2012); therefore, we did not attempt this detailed analysis.

IR pumping is an efficient mechanism to excite water molecules. In particular, the absorption of far-IR photons at 75.4 μm leads o-water molecules to the 3_{21} energy level (González-Alfonso et al. 2010). In UGC 05101 and NGC 7582, the o-H_2O $3_{21} - 3_{12}$ line at 1163 GHz is the brightest water line in the observed frequency range. Thus, in these two galaxies, IR pumping may be important for the excitation of water. On the contrary, in NGC 3227 and NGC 7130 this line is not detected, hence the contribution of IR pumping for water excitation in these galaxies could be lower.

7.2. OH^+

The formation of OH^+ is generally associated with X-ray/cosmic-ray ionizations, although it is also formed in the transition region from ionized to molecular gas in PDRs (e.g., Sternberg & Dalgarno 1995; Hollenbach et al. 2012). This molecule is detected in the spectra of galaxies, in absorption in Arp 220 (Rangwala et al. 2011; González-Alfonso et al. 2012) and M 82 (Kamenetzky et al. 2012), and in emission in the Seyfert galaxies NGC 1068 (Spinoglio et al. 2012) and Mrk 231 (van der Werf et al. 2010). Its detection is interpreted as an indication of XDR excitation in these galaxies.

Three OH^+ lines are detected in emission in the SPIRE/FTS spectrum of NGC 7130, suggesting the presence of an XDR in this galaxy. The hyperfine structure of these lines is not resolved with the spectral resolution of SPIRE/FTS; therefore, we measured the sum of the fluxes of the hyperfine transitions (Table 4).

The Einstein coefficients of the hyperfine transitions were obtained from the Cologne database for molecular spectroscopy (Müller et al. 2005). They were averaged for each fine structure level: $A_{ul} = \sum_{ij} g_i A_{ij} / \sum_i g_i$, where i and j correspond to each hyperfine upper and lower levels, respectively. Then, the transition probabilities for the 909, 971, and 1033 GHz OH^+ transitions are 1.57×10^{-2}, 1.82×10^{-2}, and 2.11×10^{-2} s^{-1}, respectively.

Using Equation (3), we determined that the beam-averaged column densities for NGC 7130 are 1.7×10^{11}, 1.7×10^{11}, and 1.6×10^{11} cm^{-2} for the upper levels of the 909, 971, and 1033 GHz lines (assuming an 18″ beam).

8. CONCLUSIONS

We presented the sub-mm spectra of 11 active galaxies observed with SPIRE/FTS. Our study is focused on the spectral lines tracing the cold and warm molecular gas phases in these galaxies. Specifically, the CO ladder from $J_{up} = 4$ to 13 lies in this spectral range, as well as the two fine structure [C I] lines at 492 and 809 GHz. For a few galaxies, we also detected HF, H_2O, and OH^+ lines. In addition, we analyzed new IRAM 30 m observations of the CO $J = 1$–0 and $J = 2$–1 transitions for three of these galaxies. The main results are summarized as follows.

1. We modeled the CO SLED (from $J_{up} = 1$ to $J_{up} = 7$–12) of six Seyfert galaxies in our sample using the escape probability approximation. For five of them, the kinetic temperature and H_2 density of the warm molecular gas are similar ($n_{H_2} \sim 10^{3.2}$–$10^{3.9}$ cm^{-3} and $T_{kin} \sim$ 300–800 K). This warm molecular gas seems to be the same gas traced by the mid-IR H_2 S(1) 17.03 μm rotational line. The heating mechanism of the warm gas is not determined since PDR, XDR, and shocks model can be combined to explain the observed CO SLEDs. However, it is likely related to the star formation activity since the L_{CO} is related to the IR luminosity but not to the AGN luminosity in these Seyfert galaxies.
2. We also used a radiative transfer model to interpret the [C I] emission. The contribution from the warm molecular gas to the [C I] emission seems to be small in these galaxies. Conversely, this emission can arise from cold ($T_{kin} < 30$ K) and dense ($n_{H_2} > 10^3$ cm^{-2}) molecular gas where the [C I] lines are thermalized. The C^0 abundance with respect to H_2 is 3×10^{-5}–8×10^{-4}; therefore, the C^0/CO abundance ratio is 0.1–2, comparable to that observed in starburst galaxies. The [C I]492 GHz/CO $J = 1$–0 ratio ranges between 15 and 85 in our galaxies. It is consistent with that expected in PDRs, although for NGC 4388 XDR excitation could be possible.
3. In two galaxies, we detected the HF $J = 1$–0 transition at 1232 GHz. In UGC 05101, it is detected in absorption and implies a column density $N_{HF} > (1.3, \pm 0.3) \times 10^{14}$ cm^{-2}. In NGC 7130, the HF transition is observed in emission. We proposed three excitation mechanisms, near-IR pumping, chemical pumping, and electron collisions, that can produce the HF $J = 1$–0 emission. From our analysis, the three mechanisms seem to be plausible. They require very dense molecular gas, and, for the IR or chemical pumping, strong near-IR or UV fields. These conditions suggest that the HF emission in NGC 7130 is associated with the AGN activity.
4. We are not able to apply any radiative model to the water emission. However, the detection of the o-H_2O 3_{21}–3_{12} transition at 1163 GHz suggests that IR pumping (due to strong far-IR continuum) could play an important role in the excitation of water molecules in some of these galaxies.
5. In NGC 7130, we detected three OH^+ lines in emission (1_0–0_1 at 909 GHz, 1_2–0_1 at 972 Ghz, and 1_1–0_1 at 1033 GHz). We derived a column density of $\sim 1.7 \times 10^{11}$ cm^{-2} for the upper levels of these three transitions. These detections suggest the presence of an XDR in NGC 7130.

We thank Rui-Qing Mao for kindly providing their published CO $J = 3$–2 data for NGC 3227 and NGC 3982. We are grateful to N. Sacchi, D. Truco, and the IRAM 30 m staff for their support during the observations. We thank the referee for comments that improved the paper. This work has been funded by the Agenzia Spaziale Italiana (ASI) under contract I/005/11/0.

SPIRE has been developed by a consortium of institutes led by Cardiff University (UK) and including University of Lethbridge (Canada); NAOC (China); CEA, LAM (France); IFSI, University of Padua (Italy); IAC (Spain); Stockholm Observatory (Sweden); Imperial College London, RAL, UCL-MSSL, UKATC, University of Sussex (UK); and Caltech, JPL, NHSC, University of Colorado (USA). This development has been supported by national funding agencies: CSA (Canada); NAOC (China); CEA, CNES, CNRS (France); ASI (Italy); MCINN (Spain); SNSB (Sweden); STFC, UKSA (UK); and NASA (USA). This research has made use of the NASA/IPAC Extragalactic Database (NED) which is operated by the Jet Propulsion Laboratory, California Institute of Technology, under contract with the National Aeronautics and Space Administration.

REFERENCES

Aalto, S., Booth, R. S., Black, J. H., & Johansson, L. E. B. 1995, A&A, 300, 369
Albrecht, M., Krügel, E., & Chini, R. 2007, A&A, 462, 575
Alonso-Herrero, A., Pereira-Santaella, M., Rieke, G. H., & Rigopoulou, D. 2012, ApJ, 744, 2
Armus, L., Charmandaris, V., Bernard-Salas, J., et al. 2007, ApJ, 656, 148
Baan, W. A., Henkel, C., Loenen, A. F., Baudry, A., & Wiklind, T. 2008, A&A, 477, 747
Black, J. H., & van Dishoeck, E. F. 1991, ApJL, 369, L9
Bolatto, A. D., Jackson, J. M., & Ingalls, J. G. 1999, ApJ, 513, 275
Brightman, M., & Nandra, K. 2011, MNRAS, 413, 1206
Cappi, M., Panessa, F., Bassani, L., et al. 2006, A&A, 446, 459
Carroll, T. J., & Goldsmith, P. F. 1981, ApJ, 245, 891
Dasyra, K. M., Ho, L. C., Armus, L., et al. 2008, ApJL, 674, L9
Davies, R. I., Thomas, J., Genzel, R., et al. 2006, ApJ, 646, 754
Deo, R. P., Crenshaw, D. M., Kraemer, S. B., et al. 2007, ApJ, 671, 124
de Vaucouleurs, G. 1975, SSS, 9, 557
Díaz-Santos, T., Alonso-Herrero, A., Colina, L., et al. 2010, ApJ, 711, 328
Downes, D., & Solomon, P. M. 1998, ApJ, 507, 615
Draine, B. T. 1978, ApJS, 36, 595
Draine, B. T. 2011, Physics of the Interstellar and Intergalactic Medium (Princeton, NJ: Princeton Univ. Press)
Falcke, H., Wilson, A. S., & Simpson, C. 1998, ApJ, 502, 199
Farrah, D., Bernard-Salas, J., Spoon, H. W. W., et al. 2007, ApJ, 667, 149
Flower, D. R., & Pineau Des Forêts, G. 2010, MNRAS, 406, 1745
Fulton, T. R., Baluteau, J.-P., Bendo, G., et al. 2010, Proc. SPIE, 7731, 773134
Genzel, R., Lutz, D., Sturm, E., et al. 1998, ApJ, 498, 579
Glover, S. C. O., Federrath, C., Mac Low, M.-M., & Klessen, R. S. 2010, MNRAS, 404, 2
Gondoin, P., Orr, A., Lumb, D., & Siddiqui, H. 2003, A&A, 397, 883
González-Alfonso, E., Fischer, J., Bruderer, S., et al. 2013, A&A, 550, A25
González-Alfonso, E., Fischer, J., Graciá-Carpio, J., et al. 2012, A&A, 541, A4
González-Alfonso, E., Fischer, J., Isaak, K., et al. 2010, A&A, 518, L43
González Delgado, R. M., Heckman, T., & Leitherer, C. 2001, ApJ, 546, 845
Griffin, M. J., Abergel, A., Abreu, A., et al. 2010, A&A, 518, L3
Guainazzi, M., Matt, G., & Perola, G. C. 2005, A&A, 444, 119
Heisler, C. A., Lumsden, S. L., & Bailey, J. A. 1997, Natur, 385, 700
Hernandez, A. K., & Tan, J. C. 2011, ApJ, 730, 44
Ho, L. C., Filippenko, A. V., & Sargent, W. L. W. 1997, ApJS, 112, 315
Hollenbach, D., Kaufman, M. J., Neufeld, D., Wolfire, M., & Goicoechea, J. R. 2012, ApJ, 754, 105
Ikeda, M., Oka, T., Tatematsu, K., Sekimoto, Y., & Yamamoto, S. 2002, ApJS, 139, 467
Imanishi, M., Terashima, Y., Anabuki, N., & Nakagawa, T. 2003, ApJL, 596, L167
Iono, D., Wilson, C. D., Yun, M. S., et al. 2009, ApJ, 695, 1537
Israel, F. P., & Baas, F. 2002, A&A, 383, 82
Kamenetzky, J., Glenn, J., Rangwala, N., et al. 2012, ApJ, 753, 70
Kaufman, M. J., Wolfire, M. G., Hollenbach, D. J., & Luhman, M. L. 1999, ApJ, 527, 795
Kennicutt, R. C., Jr. 1998, ARA&A, 36, 189
Lacy, J. H., Knacke, R., Geballe, T. R., & Tokunaga, A. T. 1994, ApJL, 428, L69
Le Bourlot, J., Pineau des Forêts, G., & Flower, D. R. 1999, MNRAS, 305, 802
Levenson, N. A., Weaver, K. A., Heckman, T. M., Awaki, H., & Terashima, Y. 2005, ApJ, 618, 167
Liszt, H. S. 2012, A&A, 538, A27
Lodders, K. 2003, ApJ, 591, 1220
Lumsden, S. L., Heisler, C. A., Bailey, J. A., Hough, J. H., & Young, S. 2001, MNRAS, 327, 459
Mao, R.-Q., Schulz, A., Henkel, C., et al. 2010, ApJ, 724, 1336
McClure, M. 2009, ApJL, 693, L81
Meijerink, R., Kristensen, L. E., Weiß, A., et al. 2013, ApJL, 762, L16
Meijerink, R., Spaans, M., & Israel, F. P. 2006, ApJL, 650, L103
Meléndez, M., Kraemer, S. B., Armentrout, B. K., et al. 2008, ApJ, 682, 94
Monje, R. R., Phillips, T. G., Peng, R., et al. 2011, ApJL, 742, L21
Müller, H. S. P., Schlöder, F., Stutzki, J., & Winnewisser, G. 2005, JMoSt, 742, 215
Naylor, D. A., Baluteau, J.-P., Barlow, M. J., et al. 2010, Proc. SPIE, 7731, 773116
Neufeld, D. A., Wolfire, M. G., & Schilke, P. 2005, ApJ, 628, 260
Ojha, R., Stark, A. A., Hsieh, H. H., et al. 2001, ApJ, 548, 253
Ott, S. 2010, in ASP Conf. Ser. 434, Astronomical Data Analysis Software and Systems XIX, ed. Y. Mizumoto, K.-I. Morita, & M. Ohishi (San Francisco, CA: ASP), 139
Panuzzo, P., Rangwala, N., Rykala, A., et al. 2010, A&A, 518, L37
Papadopoulos, P. P., Thi, W.-F., & Viti, S. 2004, MNRAS, 351, 147
Pappalardo, C., Bianchi, S., Corbelli, E., et al. 2012, A&A, 545, A75
Pereira-Santaella, M., Diamond-Stanic, A. M., Alonso-Herrero, A., & Rieke, G. H. 2010, ApJ, 725, 2270
Petric, A. O., Armus, L., Howell, J., et al. 2011, ApJ, 730, 28
Piconcelli, E., Bianchi, S., Guainazzi, M., Fiore, F., & Chiaberge, M. 2007, A&A, 466, 855
Pilbratt, G. L., Riedinger, J. R., Passvogel, T., et al. 2010, A&A, 518, L1
Rangwala, N., Maloney, P. R., Glenn, J., et al. 2011, ApJ, 743, 94
Reunanen, J., Kotilainen, J. K., & Prieto, M. A. 2003, MNRAS, 343, 192
Riffel, R. A., Storchi-Bergmann, T., Dors, O. L., & Winge, C. 2009, MNRAS, 393, 783
Rigopoulou, D., Papadakis, I., Lawrence, A., & Ward, M. 1997, A&A, 327, 493
Rigopoulou, D., Spoon, H. W. W., Genzel, R., et al. 1999, AJ, 118, 2625
Roussel, H. 2012, arXiv:1205.2576
Roussel, H., Helou, G., Hollenbach, D. J., et al. 2007, ApJ, 669, 959
Ruiz, M., Rieke, G. H., & Schmidt, G. D. 1994, ApJ, 423, 608
Rush, B., Malkan, M. A., & Spinoglio, L. 1993, ApJS, 89, 1
Sanders, D. B., Mazzarella, J. M., Kim, D.-C., Surace, J. A., & Soifer, B. T. 2003, AJ, 126, 1607
Sanders, D. B., Soifer, B. T., Elias, J. H., et al. 1988, ApJ, 325, 74
Schinnerer, E., Eckart, A., & Tacconi, L. J. 2000, ApJ, 533, 826
Schöier, F. L., van der Tak, F. F. S., van Dishoeck, E. F., & Black, J. H. 2005, A&A, 432, 369
Schroder, K., Staemmler, V., Smith, M. D., Flower, D. R., & Jaquet, R. 1991, JPhB, 24, 2487
Shaw, G., Ferland, G. J., Abel, N. P., Stancil, P. C., & van Hoof, P. A. M. 2005, ApJ, 624, 794
Shields, J. C., & Filippenko, A. V. 1996, A&A, 311, 393
Sofia, U. J., Lauroesch, J. T., Meyer, D. M., & Cartledge, S. I. B. 2004, ApJ, 605, 272
Spinoglio, L., Pereira-Santaella, M., Busquet, G., et al. 2012, ApJ, 758, 108
Sternberg, A., & Dalgarno, A. 1995, ApJS, 99, 565
Swinyard, B. M., Ade, P., Baluteau, J.-P., et al. 2010, A&A, 518, L4
Tielens, A. G. G. M., & Hollenbach, D. 1985, ApJ, 291, 722
Tommasin, S., Spinoglio, L., Malkan, M. A., & Fazio, G. 2010, ApJ, 709, 1257
Tommasin, S., Spinoglio, L., Malkan, M. A., et al. 2008, ApJ, 676, 836
van der Tak, F. 2012, RSPTA, 370, 5186
van der Tak, F. F. S., Black, J. H., Schöier, F. L., Jansen, D. J., & van Dishoeck, E. F. 2007, A&A, 468, 627
van der Tak, F. F. S., Ossenkopf, V., Nagy, Z., et al. 2012, A&A, 537, L10
van der Werf, P. P., Isaak, K. G., Meijerink, R., et al. 2010, A&A, 518, L42
Vila-Vilaró, B., Taniguchi, Y., & Nakai, N. 1998, AJ, 116, 1553
Weaver, K. A., Meléndez, M., Mushotzky, R. F., et al. 2010, ApJ, 716, 1151
Wilson, C. D. 1997, ApJL, 487, L49
Wilson, C. D., Petitpas, G. R., Iono, D., et al. 2008, ApJS, 178, 189
Wolfire, M. G., Hollenbach, D., & McKee, C. F. 2010, ApJ, 716, 1191
Wright, E. L., Mather, J. C., Bennett, C. L., et al. 1991, ApJ, 381, 200
Wu, Y., Charmandaris, V., Huang, J., Spinoglio, L., & Tommasin, S. 2009, ApJ, 701, 658
Xie, T., Allen, M., & Langer, W. D. 1995, ApJ, 440, 674
Yang, B., Stancil, P. C., Balakrishnan, N., & Forrey, R. C. 2010, ApJ, 718, 1062
Young, S., Hough, J. H., Efstathiou, A., et al. 1996, MNRAS, 281, 1206
Yuan, T.-T., Kewley, L. J., & Sanders, D. B. 2010, ApJ, 709, 884